Synthesis and Characterization of Fe_3O_4/ZnO and Fe_3O_4/ZnMnS Core-Shell Heterostructured Nanoparticles

by

Juan Carlos Beltran Huarac

A thesis submitted in partial fulfillment of the requirements for the degree of

MASTER OF SCIENCE
in
Physics

UNIVERSITY OF PUERTO RICO
MAYAGÜEZ CAMPUS
2010

Approved by:

_____	_____
Surinder Singh, PhD Member, Graduate Committee	Date
_____	_____
Dorial Castellanos, PhD Member, Graduate Committee	Date
_____	_____
Maharaj Tomar, PhD President, Graduate Committee	Date
_____	_____
Anand Sharma, PhD Representative of Graduate Studies	Date
_____	_____
Hector Jimenez, PhD Chairperson of the Department	Date

Dedicatory

To the Living GOD of Israel, *to* my *beloved Daysi, to my dear daughter Melody and to my cozy family*

Whoso loveth instruction loveth knowledge […]

Prov. 12:1

Abstract

Currently, core-shell heterostructured nanosystems are emerging as next-generation materials due to their potential multifunctionalities in contrast with the more limited single-component counterparts. Systematic investigation of core-shell nanostructures of ZnO and bare-and-doped-Mn^{2+} ZnS nanocrystals on the surface of magnetite nanoparticles (Fe_3O_4) was performed. The magnetite cores were prepared via the co-precipitation method and were next treated with an appropriate surfactant. The Fe_3O_4/(S) (S=ZnO and ZnMnS) core-shell nanoparticles were obtained by an aqueous solution method at room temperature. The structural tests were carried out using an x-ray diffractometer (XRD) which showed the development of crystalline phases of cubic Fe_3O_4, hexagonal ZnO wurtzite and cubic ZnS. These patterns also established the matching between bare and doped-Mn^{2+} ZnS diffraction peaks. Broadness of the diffraction peaks evidenced the formation of nanosize phases. The transmission electron microscopy (TEM) confirmed the deposition of a semiconductor shell on the surface of superparamagnetic Fe_3O_4 nanoparticles. The UV-Vis spectra showed the presence of a strong absorption peak and photoluminescence (PL) spectra displayed the emission peak due to excitonic recombination and a very weak defect-related emission peak suggesting the rearrangement of electronic configuration in the core-shell structures when ZnO is surrounding the core. These spectra also displayed the strong emission peak attributed to paramagnetic ion Mn^{2+} when acted as dopant in the host ZnS structure. The study of the magnetic properties was carried out using a vibrating sample magnetometer (VSM) which evidenced considerable drop in the saturation magnetization of the Fe_3O_4/ZnO nanoparticles in comparison to individual Fe_3O_4 ones. For the Fe_3O_4/ZnMnS system a slight ferromagnetic behavior at room temperature was observed. The chemical composition of these nanomaterials was performed by x-ray photoelectron spectroscopy (XPS). This elemental analysis demonstrated the presence of Zn on the surface of the magnetic seed at an appropriate shell thickness. These core-shell heterostructured nanoparticles are receiving great potential applications in biomedical areas such as photodynamic therapy.

Resumen

Los nanosistemas heteroestructurados núcleo-cáscara están actualmente emergiendo como materiales de última generación debido a sus potenciales multifuncionalidades en comparación a los sistemas homogéneamente estructurados. En este trabajo se llevó cabo una investigación sistemática de las nanopartículas núcleo-cáscara de ZnO y ZnS puro y dopado con Mn^{2+} sobre la superficie de magnetita (Fe_3O_4). Los núcleos de magnetita fueron preparados mediante el método de co-precipitación y luego fueron tratados con un surfactante adecuado. Las nanopartículas de Fe_3O_4/(S) (S=ZnO and ZnMnS) fueron obtenidas por medio de un método de solución acuosa a temperatura ambiente. Se usó un difractómetro de rayos x (XRD) para realizar las pruebas estructurales las cuales mostraron el desarrollo de las fases de Fe_3O_4 cúbica, wurtzita ZnO hexagonal y ZnS cúbica. Estos patrones también establecieron el excelente apareo entre los picos de difracción de ZnS puro y dopado con Mn^{2+}. El ancho de los picos de difracción evidenció la formación de las fases a nanoescala. El microscopio de transmisión de electrones (TEM) confirmó la deposición de una cáscara semiconductora sobre la superficie de las nanopartículas superparamagnéticas. Los espectros de UV-Vis y fotoluminiscencia (PL) indicaron la presencia de un pico de absorción y emisión intenso debido a la recombinación excitónica y un pico de emisión débil relacionada al defecto sugiriendo el re arreglo de la configuración electrónica en las estructuras núcleo-cáscara cuando el ZnO está sobre la superficie del núcleo. Estos espectros también mostraron un pico de emisión intensa atribuido al ion paramagnético Mn^{2+} cuando este actúa como dopante en la estructura de ZnS. El estudio de las propiedades magnéticas fue realizado usando un magnetómetro de muestra vibrante (VSM) el cual evidencio la disminución en magnetización de saturación de Fe_3O_4/ZnO en comparación a las nanopartículas de Fe_3O_4 individuales. Para el sistema Fe_3O_4/ZnMnS un ligero comportamiento ferromagnético fue observado a temperatura ambiente. La composición química de estos nanomateriales fue llevada a cabo mediante espectroscopia de fotoelectrones de rayos x (XPS). Este análisis elemental demostró la presencia de Zn sobre la superficie del núcleo con un grosor de cáscara apropiado. Estas nanopartículas heteroestructuradas núcleo-cáscara están recibiendo numerosas aplicaciones en áreas biomédicas como en terapia fotodinámica.

Acknowledgement

The author is grateful to all people inside and outside Mayagüez Campus for their unselfish advice and help. I really acknowledge the immeasurable patience that they brought me and the valuable time that they dedicated towards my thesis. This work is the fruit of a joint effort. I would like to express my sincere gratitude to: Drs. Maharaj Tomar and Surinder Singh for allowing me to belong to their work team, Dr. Oscar Perales for the facilities and access to his equipment, Dr. Esteban Fachini for his collaboration in XPS and SEM-EDS measurements, Dr. Guinel for his help in TEM measurements, Dr. Kumar for his cooperation in VSM measurements, Mr. Omar Vasquez for his collaboration in PL measurements, my friends Danilo and Martin for their frank friendship and CREST project for its support.

Table of Contents

Dedicatory ii

Abstract iii

Resumen iv

Acknowledgements v

Table of Contents vi

List of Tables viii

List of Figures ix

Chapter 1: Introduction 12

Reference 13

Chapter 2: Literature Survey 14

2.1 Quantum Dot 14

2.2 Core-Shell Structures 14

2.3 Theoretical Background of the Quantum Dots 17

2.3.1 General Description of the Quantum Dots 17

2.3.2 Core-Shell Quantum Dots 18

2.3.3 Surface Modification and Bioconjugation of the Quantum Dots 23

Reference 25

Chapter 3: Proposed Research 27

3.1 Rationale of Fe_3O_4/ZnO 27

3.2 Rationale of Fe_3O_4/ZnMnS 31

Reference 35

Chapter 4: Experimental Details 36

4.1 Synthesis of the Quantum Dots 36

4.2 Fe_3O_4/ZnO Quantum Dots 36

4.2.1 Synthesis 36

4.2.2 X-Ray Diffraction Measurements 38

4.2.3 TEM Measurements 42

4.2.4 UV and PL Measurements 44

4.2.5 VSM Measurements 47

4.2.6 XPS Measurements 48

4.3 Fe_3O_4/ZnMnS Quantum Dots 49
4.3.1 Synthesis 49
4.3.2 XRD Measurements 50
4.3.3 TEM Measurements 51
4.3.4 PL Measurements 52
4.3.5 VSM Measurements 54
Reference 56
Chapter 5: Conclusions 57
5.1 Findings of the Present Work and Comparison with Other Works 57
5.2 Future Perspective 59
Reference 61

List of Tables

Tables		Page
1	Variation of the average crystallite sizes for Fe_3O_4 changing the temperature and degree of agitation.	**40**
2	Variation of average crystallite size and their respective shell thicknesses for Fe_3O_4/ZnO as the molar ratios are increased.	**43**
3	Comparison of the singlet oxygen quantum yield ($^1O_2$ Φ_Δ) (PS: photosensitizer and QDs: quantum dots)	**61**

List of Figures

Figures		Page
1	Photoluminescence spectra for core-shell quantum dots and its corresponding profile [4].	**15**
2	Profile for a core-shell heterostructure	**16**
3	Band diagram for a type-I core-shell quantum dot.	**19**
4	Band diagram for a type-II core-shell quantum.	**19**
5	Schematic depiction showing step by step the light absorption in the UV-Vis region, the carrier separation and recombination and the light emission in the Vis-IR region.	**21**
6	Photoluminescence (right) and UV-Vis absorption (left) spectra for the CdTe/CdSe quantum dots showing the growth kinetics of the CdSe shell with monitored time and compared with the CdTe core [19].	**22**
7	Schematics of a magnetic/luminescent core-shell quantum dot system for photodynamic therapy. Nanoparticle is functionalized with targeting ligands in order that this to be conducted towards tumor cells. The photosensitizers are also coupled and with help of certain irradiation it get excited causing singlet oxygen from surrounding molecular oxygen which is the main agent to provoke the cellular death (slightly modified [20]).	**24**
8	Treated-citric-acid Fe_3O_4 nanoparticles showing a good dispersion [3].	**28**
9	X-ray diffraction patterns for Fe_3O_4 (a), sodium citrate modified Fe_3O_4 (b), Fe_3O_4/ZnO and ZnO nanoparticles [5].	**29**
10	TEM images for Fe_3O_4/ZnO nanoparticles before (left) and after (right) treating the surface [5].	**30**
11	M-H curves at different molar ratios, 2→6 decreases the ZnO quantity in the synthesis process [5].	**31**
12	X-ray diffraction patterns for Fe_3O_4 (a) and Fe_3O_4/ZnS microspheres [8].	**32**
13	(a) TEM, (b) HRTEM images of Fe_3O_4/ZnS; (c) FeS particles and (d), (e) and (f) subsequent reactions for 2h, 4h and 6h respectively [9].	**33**
14	Magnetic responses at 300 K for Fe_3O_4 (black) and Fe_3O_4/ZnS (red)	**34**

microspheres [9].

15 Flow chart for the preparation of magnetite. The red letters represent the parameters that were used to change the size. **37**

16 Flow chart for the synthesis of Fe_3O_4/ZnO. **38**

17 X-ray diffraction patterns for Fe_3O_4 with different synthesis conditions. **39**

18 X-ray diffraction spectra for ZnO (a), Fe_3O_4 (b) and Fe_3O_4/ZnO (c). **41**

19 X-ray diffraction patterns for Fe_3O_4 before and after treatment showing none change through the modification with sodium citrate. **41**

20 TEM figures for the Fe_3O_4/ZnO particles with R=1:2 corroborating the size at nanoscale. The contrast in core and shell images verifies the core-shell structure. **42**

21 Size distribution for the particles of Fe_3O_4/ZnO. It can be observed that occurrence maximum peak is just at 15 nm as approximately calculated with the eq. 4.1 (see Table 2). **43**

22 Optical absorption spectra for ZnO (black) and Fe_3O_4/ZnO (red). **44**

23 Absorption spectra for Fe_3O_4/ZnO at different molar ratio in comparison to pure ZnO. **45**

24 Photoluminescence spectra for ZnO (a) and R=1:2 (b), R=1:3(c) and R=1:5(d) Fe_3O_4/ZnO nanoparticles. **45**

25 Optical absorption and photoluminescence spectra for pure ZnO and Fe_3O_4/ZnO (left) and photographs obtained by exposing a UV lamp on the samples: Fe_3O_4 (black), Fe_3O_4/ZnO (brown) and ZnO (yellow). **46**

26 M-H curves for Fe_3O_4 (59.87 emu/g) and Fe_3O_4/ZnO (15.64 emu/g) nanoparticles (left) and photographs of the samples obtained by a UV lamp and a permanent magnet: Fe_3O_4 (black) and Fe_3O_4/ZnO (brown). **47**

27 M-H curves for Fe_3O_4 and R=1:2, R=1:3 and R=1:5 Fe_3O_4/ZnO nanoparticles at different molar ratios. **48**

28 Surface chemistry of Fe_3O_4/ZnO nanoparticles obtained by x-ray photoelectron spectroscopy suggesting the presence of Zn on the surface of core material. **49**

29 Flow chart for the preparation of Fe_3O_4/ZnMnS. **50**

30 X-ray diffraction patterns showing the formation of both Fe_3O_4 and ZnS phases in the $Fe_3O_4/Zn_{1-x}Mn_xS$ core-shell heterostrucutures with x=0.20 and x=0.25. **51**

31 TEM images for Fe_3O_4/ZnMnS at magnifications of 50 and 10 nm. The **52**

contrast in core and shell images verifies the core-shell structure.

32 Size distribution for the particles of Fe_3O_4/ZnMnS. It can be observed that occurrence maximum peak is just at 14 nm as approximately calculated from XRD measurements. **52**

33 Photoluminescence spectra for $Fe_3O_4/Zn_{1-x}Mn_xS$ (x=0.20, 0.25) compared with bare and doped-Mn^{2+} (x=0.10) ZnS (left). Strong emission peaks for doped ZnS at different concentrations with an inset indicating the dopant energetic level (right). **53**

34 Schematics for the band structure of Fe_3O_4/ZnS with real sizes (left) and photographs of the samples obtained by a UV lamp: Fe_3O_4 (black), ZnS(gray), $Fe_3O_4/Zn_{0.75}Mn_{0.25}S$ (orange) and $Zn_{0.90}Mn_{0.10}S$ (ligh orange). **54**

35 M-H curves for Fe_3O_4 (42.29 emu/g) and $Fe_3O_4/Zn_{1-x}Mn_xS$ with x=0.25 (5.21 emu/g). The inset shows the magnification of the same figure around the origin suggesting a slightly ferromagnetic behavior at room temperature (left) and photographs of the samples obtained by a UV lamp and a permanent magnet: Fe_3O_4 (black) and $Fe_3O_4/Zn_{0.75}Mn_{0.25}S$ (orange). **55**

36 A comparison of x-ray diffraction patterns for Fe_3O_4/ZnO of others and our work, from left to right: Wan et al. [1] with A: Fe_3O_4 and B: Fe_3O_4/ZnO; Zou et al. [2] with (a): Fe_3O_4 and (b), (c) and (d): Fe_3O_4/ZnO at increasing molar ratios; and present work with (a): ZnO, (b) Fe_3O_4 and (c) Fe_3O_4/ZnO. **57**

37 A comparison of M-H curves at room temperature for Fe_3O_4/ZnO of others and our work, from left to right: Wan et al.[1] with 31.25 emu/g; Hong et al. [3] with (6): 20.33, (5): 17.12, (4): 13.67, (3): 9.72 and (2): 5.52 emu/g at increasing molar ratios; and present work with 15.01, 9.63 and 7.72 emu/g at R=1:2; 1:3 and 1:5 respectively. **58**

Chapter 1: Introduction

The concern for materials at nanoscale (1nm = 10^{-9} m) arises from the fact that materials show new optical, electrical and magnetic properties at this length regime and change with their composition, shape and size. So, what does the term "nano" imply? If we diminish the size of a material, at what point does it begin to act more like an atom or molecule? or, in the case of a cluster, how many atoms do we have to add observing a bulk-like behavior? [1]. It can certainly be assured that nanomaterials represent a bridge between single molecules and bulk materials. Thus, their structures and properties vary substantially from those of atoms, molecules and bulk systems. Therefore, nanoscale phenomena are interesting to physicists, chemists and biologists.

The phrase "nanostructure" refers to clusters, nanoparticles, quantum dots, nanowires and nanotubes. The clusters designate small and multi-atom particles between 3 and $3x10^7$ atoms. The term "nanoparticles" belongs to the particles in the range of 1 to 100 nm in diameter. Each nanoparticle in a crystalline arrangement may be either a single crystal or polycrystalline [2]. In quantum dots, also known as inorganic semiconductor nanocrystallites or "artificial atoms", the electron-hole pairs are confined in all three spatial dimensions. The quantum confinement effect is prominent in the quantum dots having their size smaller than their corresponding Bohr radius.

Nanoscale heterostructures have received a great deal of interest because they provide degrees of freedom for tuning the physical and chemical properties of the material. A case of characteristic heterostructures synthesized are colloidal core-shell nanomaterials differing from homogeneous ones by the fact that their physical and chemical properties are driven by an interface between two materials and provides multifunctionality that strongly depends on the appropriate choice of the core size and shell thickness. The assembly of these core-shell quantum dots results in thermal and chemical stability, better solubility, less cytotoxicity and ease in bioconjugation [3]. In addition, the shell material can prevent the oxidation of the core material and permit a rearrangement in electron configuration of the whole system.

Accordingly, in this work a systematic research is directed to understand the optical and magnetic properties of core-shell nanostructures, where superparamagnetic Fe_3O_4 nanoparticle

forms the core with the shell of ZnO and ZnS: Mn^{2+}. The II-VI semiconductor shell with varying thickness endowed with photoluminescence to the superparamagnetic core passivating the surface defects and confining the electron-hole pairs towards a particular region of these heterostructures [4]. We synthesized and investigated core-shell heterostructures of Fe_3O_4/ZnO and Fe_3O_4/ZnMnS with well-defined structural, morphological, optical absorption, photoluminescence and magnetic properties as well as its surface chemistry for further functionalization. The common properties of both systems in core-shell quantum dots are novel and attractive due to their great potential for applications in biomedical science, in particular photodynamic therapy and *in situ* tumor treatment.

The following chapters describe the particular sequence with a title related to this thesis work. Chapter 2 presents the survey of basic and necessary background to figure out qualitative and quantitative reasons for which the core and shell materials were chosen. The up-dated literature of the past related research based on Fe_3O_4/ZnO and Fe_3O_4/ZnMnS core-shell quantum dots is elucidated in Chapter 3. Chapter 4 is intended to explain how the core-shell structures were synthesized from easily reproducible stages by step evolution. It also contains important results with their respective discussions and their multifunctional properties. In Chapter 5 we included the comparison of our research results with other works and we also give some future perspective.

Reference

[1] Kenneth J. Klabunde and Ryan M. Richards, "*Nanoscale materials in chemistry*", JOHN WILEY & SONS, New Jersey, **2009**, 2nd Ed., chapter 1.

[2] Robert Kelsall, Ian Hamley and Mark Geoghegan, "*Nanoscale Science and Technology*", John Wiley & Sons, Ltd, England, **2005**, chapter 1.

[3] C.N.R. Rao, A. Müller, A.K. Cheetham, "*The chemistry of Nanomaterials*", WILEY-VCH Verlag GmbH & Co. KgaA, Weinheim, **2004**, chapter 12.

[**4**] Peter Reiss, Myriam Protière and Liang Li, "Core-Shell Semiconductor Nanocrystals", *Small Journal* (**2009**) 5(2): 154-168.

Chapter 2: Literature Survey

2.1 Quantum Dot

Colloidal semiconductor nanocrystals or quantum dots constitute the building blocks for novel materials that are essential for emerging technologies. The interesting physical and chemical properties in these nanosystems arise as a result of small size and quantum confinement effects. The quantum dots possess high surface to volume ratio which give rise to enhanced chemical activity. Their sizes are typically in the range of 1-100 nm. More specifically, the dimension of the quantum dot is less than the De Broglie wavelength of thermal electrons [1],

$$\lambda = \frac{h}{(2m_e k_B T)^{1/2}} \approx 7.6\, nm \qquad (2.1)$$

where m_e is the electron mass and k_B is Boltzmann's constant at room temperature. Thus, the quantum effects in the quantum dots are expected to occur. In addition, the band gap at this scale depends on the size a_o of the quantum dot [2] as evidenced by,

$$E_g(a_o, n, L) \approx E_g^{bulk} + \frac{2\hbar^2 \varphi_{nL}^2}{a_o^2}\left(\frac{1}{m_e^*} + \frac{1}{m_h^*}\right) \qquad (2.2)$$

with φ_{nL} representing the roots of the spherical Bessel functions and m_e^* and m_h^* the effective masses of the electrons and holes respectively suggesting that the density of states increases as nanocrystal size is bigger. Thus, we can modify the physical and chemical properties of the quantum dots by changing their sizes. An alternative, say, is to make core-shell heterostructures since the sizes of core and shell can be varied. This allows reducing the surface defects and provoking the rearrangement of electrons that affect the optical properties significantly.

2.2 Core-Shell Structures

It is well known that the most of fluorescent proteins and organic dyes suffer from photobleaching; however, by utilizing a core-shell quantum dot system, this drawback could be

solved and certain stability against photobleaching could be added without losing their luminescent attributes [3]. Figure 1 shows as the appropriate selection of the shell material affects substantially the photoluminescence of the core material and promotes the multifunctionality. In system 1 a strong emission peak is observed because the core bandgap is lower, while in system 2 it is suppressed due to higher core bandgap.

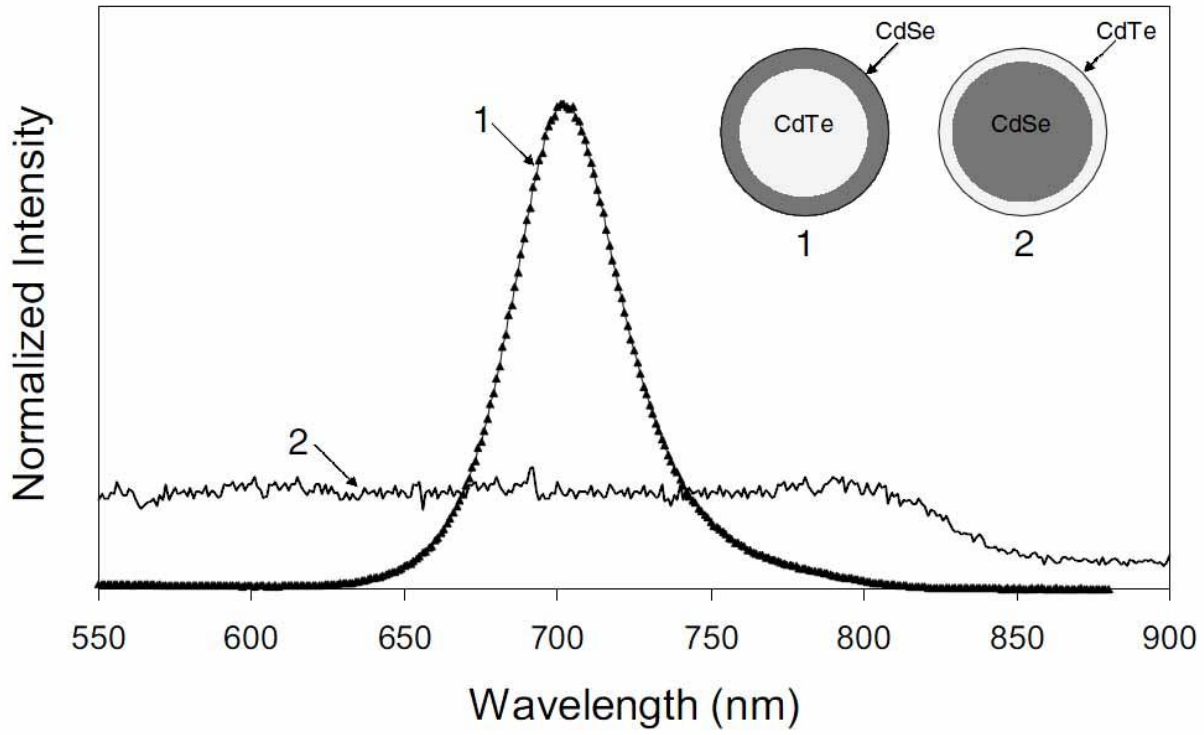

Figure 1: Photoluminescence spectra for core-shell quantum dots and its corresponding profile [4].

The key advantage in synthesizing core-shell nanostructures lies in the fact that we can manipulate at will their physical properties by changing size of core and shell and combine the multifunctionality. Their sizes range from around 20 to 200 nm in diameter. An enormous diversity in exotic properties (Figure 2) can be obtained from these nanostructures varying from fillers, pigments, coatings to highly sophisticated nanosensors for cellular imaging and carriers of photosensitizing agents in photodynamic therapy [5].

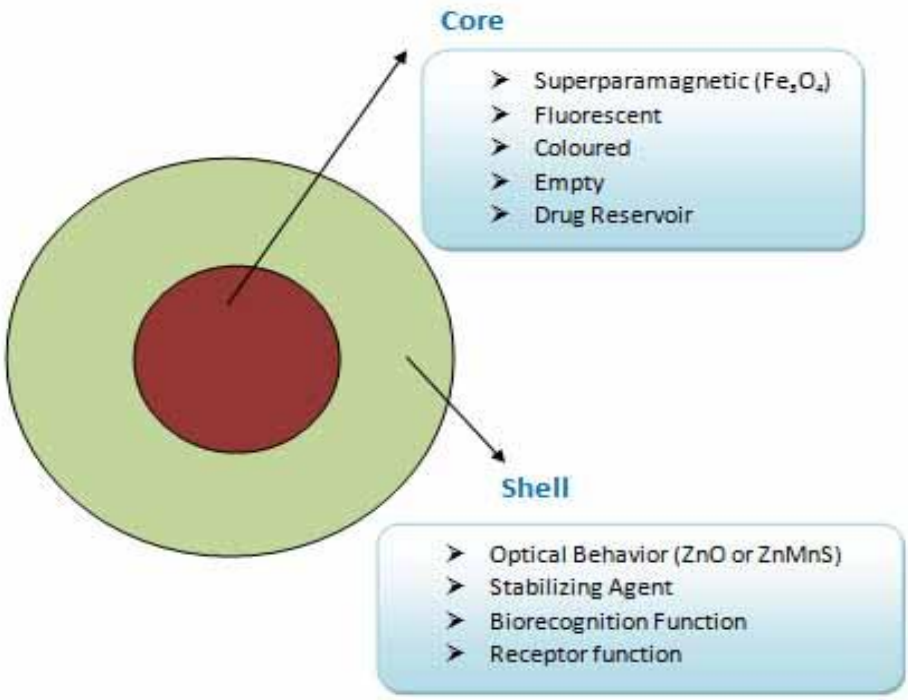

Figure 2: Profile for a core-shell heterostructure.

Unlike the standard quantum dots (single nanoparticles), in the core-shell structures both the shell thickness and the core diameter tune chemical and physical properties such as optical properties (emission). In addition, if by assembling these nanostructures the spatial separation of carriers is possible; their properties will be ruled by the band offset of the comprising materials. Thus, this system can emit energies that are different than that of the shell material. In another way, the band engineering can permit optical transitions that are forbidden and the difference in band gap of comprising materials would constitute a critical parameter to improve the photoluminescence of the system.

In the case of semiconductor quantum dots, it is usually chosen a shell material with wider bandgap than that of the core material in order to diminish their interaction with the surface traps and avoid the shell material to absorb the light emitted by the core material. The aim of this shell layer is to passivate the surface nonradiative emission enhancing the photoluminescence quantum yield and preventing natural degradation [6]. In the inverted core-shell quantum dots, the shell material has a narrower bangap than that of the core yielding a separation of the carriers.

2.3 Theoretical Background of the Quantum Dots

2.3.1 General Description of the Quantum Dots

As it has been already stated, the extraordinary optical properties in the quantum dots arise due to the quantum confinement effects that modify the processes of intraband and interband relaxation [7]. Such processes are governed by the dynamics of the excitons which arise as a result of the promotion of an electron from the valence band towards the conduction band leaving behind a hole with the same charge but opposite in the valence band [8]. Thus, these opposite charges obey the Coulomb interaction and depending on the intensity of this interaction, the optical transitions could be manipulated. But to describe physically this process, we need a model to understand the dynamics of this electron-hole pair within the nanocrystal. We are forced to invoke the quantum mechanics and seek for a suitable model that illustrates this phenomenon. If we suppose that this nanocrystal has spherical shape with radius R, behave interiorly as a uniform medium and the excitons are localized with infinite potential outside the nanocrystal [9]. Then the particle-in-a-box quantum model fits excellently with this system; the box walls acting as the nanocrystal surface. So, Brus et al. making use of the effective mass approximation, the electrostatic potential for dielectric polarization, in cases of small effective mass, the penetration of carriers outside the nanocrystal and the Schrödinger equation proposed the following Hamiltonian for the electron-hole pair [10],

$$H = -\frac{h^2}{8\pi^2}\left(\frac{\nabla_e^2}{m_e} + \frac{\nabla_h^2}{m_h}\right) + \hat{V}(\bar{S}_e, \bar{S}_h), \quad \hat{V} = \begin{cases} 0, & r \leq R \\ \infty, & r \geq R \end{cases} \tag{2.3}$$

where r is the distance from the center of the nanocrystal, m_e and m_h are the effective masses of the electron and hole respectively and $\bar{S}_e$ and $\bar{S}_h$ are the positions of the electron and hole respectively within nanocrystal. Here the determining factor is the potential energy containing several terms but the prevailing factor within the nanocrystal is the Coulomb interaction which considers the dielectric contribution of medium. Furthermore, the interior presence of a charge is going to polarize the nanocrystal modifying the energy of the second charge. Hence, this contribution called polarization energy also must appear in the eq. 2.3. Then, it is possible to rewrite this equation as follows,

$$H = -\frac{h^2}{8\pi^2}\left(\frac{\nabla_e^2}{m_e} + \frac{\nabla_h^2}{m_h}\right) - \frac{e^2}{4\pi\varepsilon\epsilon_0|\bar{S}_e - \bar{S}_h|} + \frac{e^2}{2}\sum_{k=1}^{\infty}\alpha_k \frac{S_e^{2k} + S_h^{2k}}{R^{2k+1}} \qquad (2.4)$$

where ε is the dielectric constant of nanocrystal, ϵ_0 is the vacuum permittivity and α_k depends on the dielectric constants inside and outside the nanocrystal. The eq. 2.4 consists of the hydrogen-like Hamiltonian of the bulk and an additional term related to the dielectric contributions. By putting this expression into the Schrödinger equation along with the proper boundary and continuity conditions, the allowed exciton energies are given by,

$$E_{exciton} = \frac{h^2}{8R^2}\left(\frac{1}{m_e} + \frac{1}{m_h}\right) - \frac{1.8e^2}{4\pi\varepsilon\epsilon_0 R} + \frac{e^2}{R}\overline{\sum_{k=1}^{\infty}\alpha_k \left(\frac{S}{R}\right)^{2k}} \qquad (2.5)$$

Note from eq. 2.4 that when *R* tends to infinite the Hamiltonian becomes the classic hydrogen-like Hamiltonian of the bulk. In an alternative way, in eq. 2.5 at *R* small, it is only observed the very energetic sum of two particles in a box [11]. Thus, that is possible to associate the size dependence of the nanocrystal to this model that facilitates the first absorption and emission characteristics.

2.3.2 Core-Shell Quantum Dots

Unlike the homogeneous quantum dots, core-shell nanoheterostructures are conducted by an interface which generates a number of unique and technologically novel physical properties. In addition, they also possess a large surface to volume ratio generating prominent surface-related phenomena. There exist two types of core-shell quantum dots depending on the relative position of the conduction and valence bands in both materials. If the positions of the conduction and valence bands of the core material are between those of the shell material, the core-shell quantum dot system will be called of type I, see Figure 3. In type-I configuration, the core material will determine the lifetime and the emission wavelength since the exciton will be confined to this material which could reduce their interaction with the surface traps [12]. The advantage of this configuration is the enhancement of the probability of radiative recombination. As in a standard quantum dot, the drawback in this configuration is the easy re-absorption of the emitted photons as absorption, thus emitting at the same energy [13].

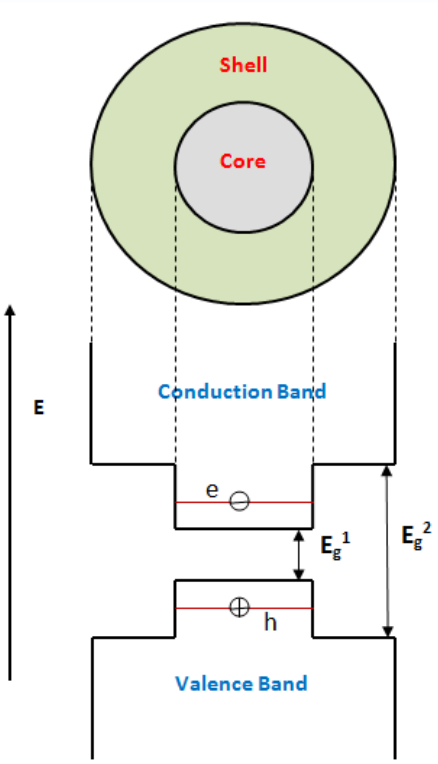

Figure 3: Band diagram for a type-I core-shell quantum dot.

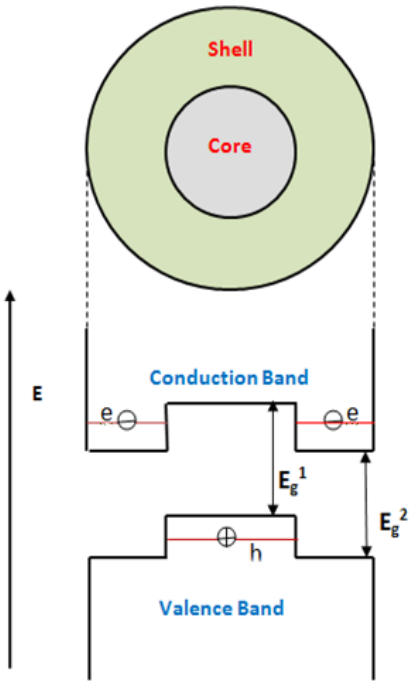

Figure 4**:** Band diagram for a type-II core-shell quantum dot.

On the other hand, the type-II core-shell quantum dots appear when the extrema of the conduction and valence bands lie in different regions of the heterostructure as in a staggered way. From Figure 4 one can observe that in this configuration it is possible a spatial separation of the carriers, namely, the hole (electron) can be within the shell material (core material) and the electron (hole) in the core material (shell material). Due to this separation, according to "Tight binding" model, the overlapping of electron and hole wavefunctions will diminish in intensity [14]. Thus, it is expected a low probability but it is possible to establish the emission transitions from both materials.

The nature of electrons and holes wavefunctions in these configurations could be understood based on a simplified model of interacting particles within a spherical box with no alloying at the interface. The calculation by Pye et al [15] of allowed energies of electrons and holes in CdSe/ZnS core-shell quantum dots has been carried out supposing that these quantum dots are ideally spherical. As in the case of a sphere, the carriers outside the quantum dot will experience an infinite potential and inside the quantum dot certain constant potential and effective mass values different for each comprising material. In this model, it is used the time-independent Schrödinger equation,

$$\widehat{H}\Psi(r,\theta,\phi) = E\Psi(r,\theta,\phi) \qquad (2.6)$$

The stationary states and an appropriate dispersion relation for this system could be obtained using above Hamiltonian. It is well-established that the solutions to the equation (2.6) with a central potential are the product of a linear combination of spherical Bessel functions and spherical Neumann functions for the radial part and the spherical harmonics for the angular part taking into account the continuity conditions and probability current at the interface [16]. Summing the energies of the carriers at the extrema of bands and the core material gap, it is possible to determine the energy for the most important optical transition [15].

On the other hand, we do not know yet how the band alignment in the type-II configuration occurs but we do know that the spatial separation of carriers make this configuration energetically favorable upon photoexcitation. With appropriately choosing the composing

materials, knowing the difference in gap energies between them and examining the structural mismatching, we can determine such separation and thus enhancing the photoluminescence efficiency. However, these established band configurations do not allow localizing the carriers within the structure accurately. Imagine that either the valence band or the conduction band of comprising materials is aligned, but the position of the other ones does not. Then, one carrier would be delocalized over the quantum dot and the other confined to either the shell or core. To the best of our knowledge, this problem has not been solved and too many speculations can be done.

From a practical point of view, we can give an possible explanation not of the phenomenon but of the main absorption of the type-II configuration since this quantum dot due to the spatial separation acts as an indirect semiconductor with its exciton decaying more slowly than that of the type-I quantum dot. The effective density of states raise when the nanocrystal size increases, then the quantum dot will experiment a slight shift in absorptivity towards the blue region with respect to the core material [17], see Figure 5. Thus, the photoluminescence will present an emission peak at longer wavelengths instead of the *customary* deep trap luminescence of the core material. This proves that the growth of a shell layer onto the surface not only quench the band-edge luminescence. With this in mind, it is not unbelievable to expect the size distribution to be broader than that of the type-I one [18].

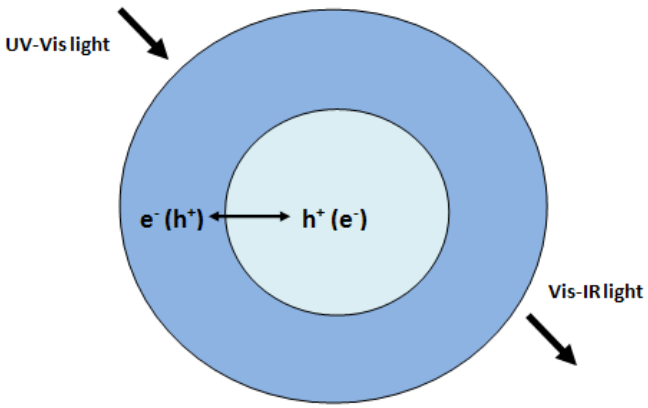

Figure 5: Schematic depiction showing step by step the light absorption in the UV-Vis region, the carrier separation and recombination and the light emission in the Vis-IR region.

To some extent, the major properties of these quantum dots are governed by their interface. In the case of the emission, the radiative recombination of the carriers is produced when these cross the interface of the core-shell system. The proper arrangement of the individual bands of the composing materials might facilitate different band gap energies. Thus, numerous probable groupings could tune these band gaps allowing the band engineering. In the CdTe/CdSe system which has been extensively studied the hole (electron) confinement energies are mostly governed by the core (shell) diameter (thickness). That is, by varying simultaneously the core diameter and shell thickness, we will obtain a joint effect that favors to the type-II system. Following this, Yu et al. [19] found a high PL efficiency in CdTe/CdSe by maintaining fixed the CdTe core and carrying out the growth kinetics of the CdSe shell gradually, see Figure 6.

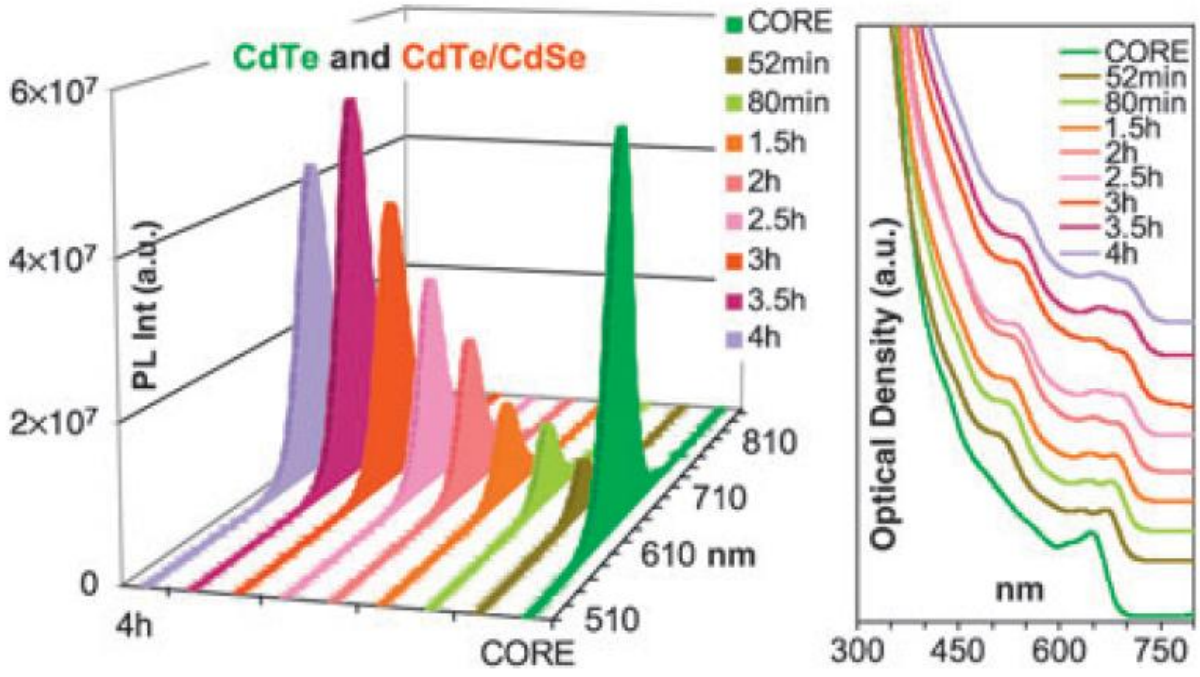

Figure 6: Photoluminescence (right) and UV-Vis absorption (left) spectra for the CdTe/CdSe quantum dots showing the growth kinetics of the CdSe shell with monitored time and compared with the CdTe core [19].

The possible *slow* recombination of the carriers in the type-II configuration can account for the longer radiative lifetimes. In the case nonradiative, these structures confine the holes (electrons) in a particular region away from the surface absorbing a significant part of traps. These traps are

present at any type of configuration. With a mismatching of band offsets, it is possible to assign an increase in the overlapping of the carrier wavefunctions which should enhance the quantum efficiency. It is thought to get the same result by smoothing the boundaries between the core and shell material [18]. But there is not much experimental work oriented to this point.

2.3.3 Surface Modification and Bioconjugation of the Quantum Dots

If these core-shell quantum dot systems with onionlike structure are thought to be used in biomedicine, we have to struggle with the problem of solubility, in particular, in aqueous media and the problem of bioconjugation. Both of them can be solved by passivating the surface appropriately with certain ligands using a proper surface modification technique in order to obtain nanocrystals capable to accept biological macromolecules on their surface and retain their excellent optical properties.

Due to the large surface to volume ratio of the quantum dots the steric hindrance, that facilitates the effective arrange of molecules onto the surface, allows a increase in the number of surface functional groups per unit surface area on the nanocrystal. This improved and strongly coordinated attaching overcomes the bulk substrates [4]. To make certain surface soluble in water, the ligand should possess molecules with polar groups that ease an effortless displacement of the quantum dots in this medium bringing it a hydrophilic character and leaving some chance for some further surface treatment. The strong bonds can be achieved by suitably polarizing the surface and exploiting at maximum the electrostatic interaction. Once functionalized, we can conveniently choose some bifunctional linker to conjugate biological molecules onto these surface groups by means of straightforwardly accessible techniques, see Figure 7.

The main attributes of these treatments ranging from avoiding high aggregation to protect against photobleaching as in the dyes. This latter one gives excellent stability to quantum dot as well as reduces the interaction with the inherent defects in the surface. In addition, this treatment makes these quantum dots less sensitive to environment changes, surface chemistry and photo-oxidation. Therefore, we can conclude this section claiming that the proficient passivation of the surface trap states provokes a robustly improved fluorescent quantum yield [21].

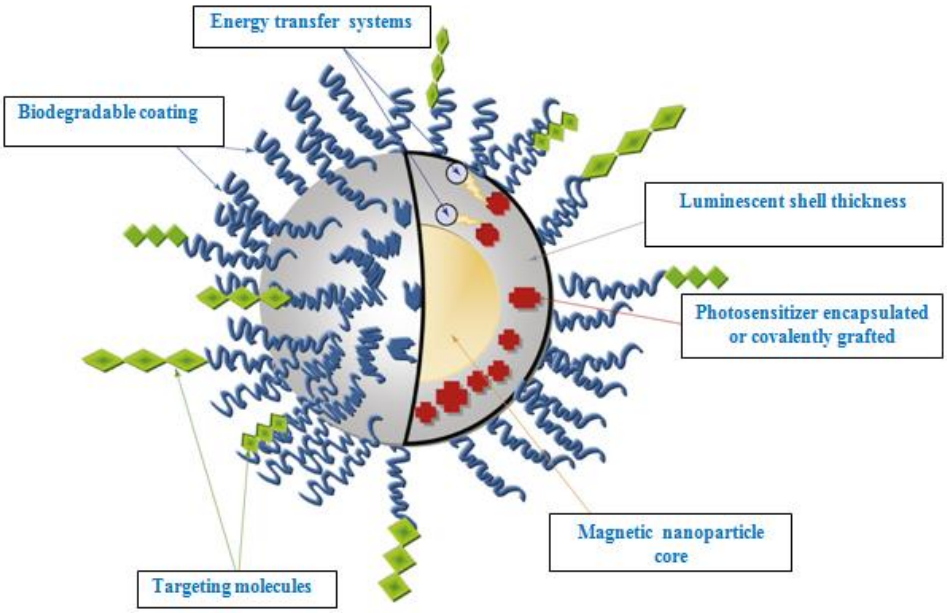

Figure 7: Schematics of a magnetic/luminescent core-shell quantum dot system for photodynamic therapy. Nanoparticle is functionalized with targeting ligands in order that this to be conducted towards tumor cells. The photosensitizers are also coupled and with help of certain irradiation it get excited causing singlet oxygen from surrounding molecular oxygen which is the main agent to provoke the cellular death (slightly modified [20]).

Reference

[1] Mark Fox, "*Quantum Optics, an Introduction*" Oxford University Press, Appendix D, **2006**.

[2] Yang Xu, "*Synthesis and Characterization of Silica Coated CdSe/CdS Core/Shell Quantum Dots*", Ph. D. Thesis, Virginia Polytechnic Institute and State University, Chapter 2, **2005**.

[3] Ruirui Zhang, Chuanliu Wu, Lili Tong, Bo Tang and Qing-Hua Xu, "Multifunctional Core-Shell Nanoparticles as Highly Efficient Imaging and Photosensitizing Agents" *Langmuir* (**2009**) 25(17): 10153-10158.

[4] C.N.R. Rao, A. Müller, A.K. Cheetham, "*The chemistry of Nanomaterials*", WILEY-VCH Verlag GmbH & Co. KgaA, Weinheim, Chapter 12, **2004**.

[5] Challa Kumar, "*Nanomaterials for Medical Diagnosis and Therapy*", Nanotechnologies for the life sciences Vol. 10, WILEY-VCH Verlag GmbH & Co. KGaA, Weinheim, Chapter 4, **2007**.

[6] B.O. Dabbousi, J. Rodriguez-Viejo, F.V. Mikulec, J.R. Heine, H. Mattoussi, R. Ober, K.F. Jensen and M.G. Bawendi, "(CdSe)ZnS Core-Shell Quantum Dots: Synthesis and Characterization of a Size Series of Highly Luminescent Nanocrystallites", *J. Phys. Chem. B* (**1997**) 101:9463-9475.

[**7**] Omar Manasreh, "*Semiconductor Heterojunctions and Nanostructures*", McGraw-Hill, Chapter 6, 2005.

[**8**] Mark Fox, "*Optical Properties of Solids*", Oxford University Press, Chapter 4, **2001**.

[9] Catherine J. Murphy and Jeffery L. Coffer, "Quantum Dots: A Primer", *Applied Spectroscopy* (**2002**) 56(1): 16A-27A.

[**10**] Louis E. Brus, "A simple model for the ionization potential, electron affinity, and aqueous redox potentials of small semiconductor crystallites" *J. Chem. Phys*. (**1983)** *79*: 5566–5571.

[11] Tadd Kippeny, Laura A. Swafford and Sandra J. Rosenthal, "Semiconductor nanocrystals: a powerful visual aid for introducing the particles in a box", *Journal of Chemical Education*, (2002) 79(9): 1094-1100.

[12] Sungjee Kim, Brent Fisher, Hans-Jürgen Eisler and Moungi Bawendi, "Type-II quantum dots: CdTe/CdSe (core-shell) and CdSe/ZnTe (core-shell) heterostructures", *J. Am. Chem. Soc.* (**2003**) 125: 11466-11467.

[13] Sergei Tretiak and Andrei Piryatinski, "Modeling photoexcited carrier interactions in semiconductor nanostructures", *Nanotechnology*, 19 September **2006**, DOI: 10.1117/2.1200608.0384.

[14] David A. Bussian, Scott A. Crooker, Ming Ying, Marcin Brynda, Alexander L. Efros and Victor I. Klimov, "Tunable magnetic exchange interactions in manganese-doped inverted core-shell ZnSe-CdSe nanocrystals" *Nature Mater.* (**2009**) 8**:** 35–40.

[15] A. Pye, "*Carrier energy levels in core-shell quantum dots*", Department of Physics, University of Surrey, England, www.surrey.ac.uk

[16] Ulrike Woggon, "*Optical Properties of Semiconductor Quantum Dots*", Springer-Verlag Berlin Heidelberg, Chapter 3, **1997**.

[17] Sergei A. Ivanov, Jagjit Nanda, Andrei Piryatinski, Marc Achermann, Laurent P. Balet, Ilia V. Bezel, Polina O. Anikeeva, Sergei Tretiak and Victor I. Klimov, "Light Amplification Using Inverted Core/Shell Nanocrystals: Towards Lasing in the Single-Exciton Regime", *J. Phys. Chem. B* (**2004**) 108: 10625-10630.

[18] Sungjee Kim, "*Novel Type-II Nanocrystal Quantum Dots and Versatile Oligomeric Phosphine Ligands*", Ph. D. Thesis, Massachusetts Institute of Technology, Chapter 2, **2003**.

[19] Kui Yu, Badruz Zaman, Svetlana Romanova, Da-shan Wang and John A. Ripmeester, "Sequential Synthesis of Type II Colloidal CdTe.CdSe Core-Shell Nanocrystals", *Small Journal* (**2005**) 1(3): 332-338.

[20] Denise Bechet, Pierre Couleaud, Céline Fronchot, Marie-Laure Viriot, François Guillemin and Muriel Barberi-Heyob, "Nanoparticles as vehicle for delivery of photodynamic therapy agents", *Trens in Biotechnology* (**2008**) 26(11): 612-621

[**21**] Peter Reiss, Myriam Protière and Liang Li, "Core-Shell Semiconductor Nanocrystals", *Small Journal* (**2009**) 5(2): 154-168.

Chapter 3: Proposed Research

The fundamental question in this section is to elucidate the construction of the core-shell structure from the synthesis of the core material with an excellent magnetic response (depending on its diameter) and a suitable surface for further functionalization. Then, the shell material is grown on the core surface. It is assumed that both core and shell materials possess diameters at the nanometric scale.

3.1 Rationale of Fe_3O_4/ZnO

Fe_3O_4 (magnetite) have proven to be a suitable material for biological applications. We have found three basic properties for using it as core material: biocompatibility, interactive functions at the surface and high magnetic saturation. In addition, the behavior at quantum scale brings a remarkable superparamagnetism at room temperature since each particle is associated to a single magnetic domain. Thus, these particles do not show any magnetism after the removal of an applied magnetic field [1].

The most common method to prepare Fe_3O_4 nanoparticles is the co-precipitation method which consists of inserting a base to an aqueous mixture of Fe^{2+} and Fe^{3+} ions at a 1:2 molar ratio with certain synthesis parameters to be controlled and adjusted to obtain particles with nanosize (this synthesis process is easy, cheap and not needs very sophisticated equipments to be carried out). The surface of these nanostructures depends on the precipitation, purification and drying mechanisms, but there exists diverse ways to treat its surface for a particular application. For instance, it is well known that these nanoparticles tend to aggregate into large cluster due to anisotropic dipolar attraction. To avoid this, they are treated with sodium citrate or any adequate organic compounds which are employed as a surfactant to create an electrostatic double layer [2]. Following this reasoning, Liu et al. obtained well-dispersed magnetite nanoparticles with almost no cluster presented (see Figure 8). The structural attributes of these nanoparticles mostly are not affected by such treatments.

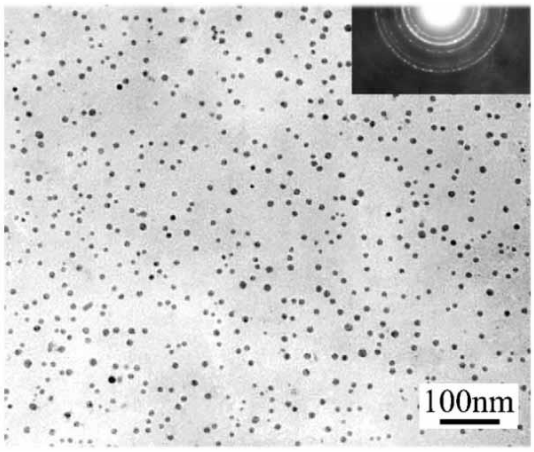

Figure 8: Treated-citric-acid Fe_3O_4 nanoparticles showing a good dispersion [3].

Once we know how to prepare and functionalize the core material, now we should assembly on these treated surfaces a layer of shell material. The choice of zinc oxide (ZnO) semiconductor as shell material is due to its high stability, tested biocompatibility and customary wide band gap (E_g ~ 3.37 eV at 300 K) and large excitonic binding energy (~ 60 meV) as well as its strong photoluminescence at room temperature. Lately, ZnO is being evaluated to confirm if this can produce cytotoxic singlet oxygen [4] which is convenient for our purposes since it will be inserted onto the treated magnetite surface to form a platform for photodynamic therapy.

The first question arising in growing ZnO onto Fe_3O_4 is the structural mismatching. It is well-known from doping in semiconductors that ionic radius is a deciding factor that must be taken into account. The cubic spinel structure of the core material (Fe_3O_4) with 3+ and 2+ valences and the hexagonal wurtzite structure of the shell material (ZnO) with valence 2+ differ into approximately 19 pm suggesting that heterogeneous nucleation can be favored if it is introduced the magnetite nanoparticles as seeds instead of a homogeneous nucleation. Consequently, in this stage is necessary to adjust rigorously the synthetic conditions in order to avoid the homogeneous nucleation of the ZnO. So then, we will only just obtain one type of nanoparticles and make sure the formation of core-shell heterostructure. But how can we do that? A possible chance to the problem is to drip slowly the solution containing the shell material into the whole solution in order not to allow the formation of other particles by means of the consumption of each drop throughout the total solution at certain time. For instance, Hong et al. [5] after redispersing sodium citrate modified Fe_3O_4 nanoparticles in water, certain quantities of dihydrate

zinc acetate in water were pertinently dripped into this solution obtaining particles with core-shell nanostructures; his results are displayed in Figure 9 indicating that both phases Fe_3O_4 and ZnO were formed.

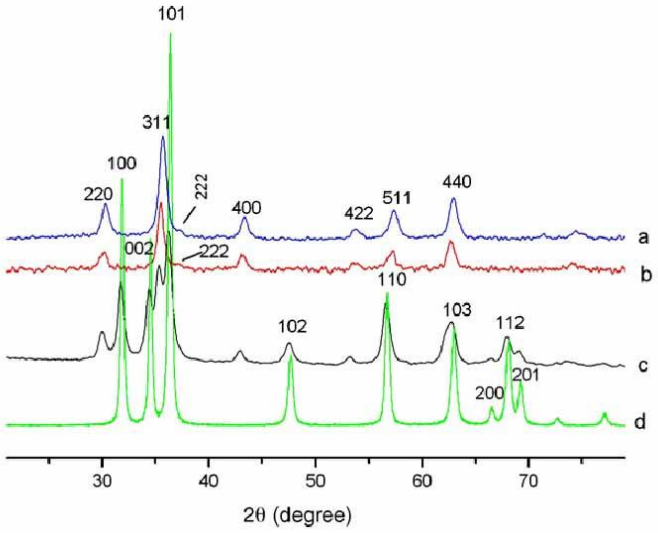

Figure 9: X-ray diffraction patterns for Fe_3O_4 (a), sodium citrate modified Fe_3O_4 (b), Fe_3O_4/ZnO and ZnO nanoparticles (d) [5]. From (a) and (b) is showed that the crystalline structure of Fe_3O_4 did not change through the surface treatment.

From figure 9 one can observe that the peaks corresponding to Fe_3O_4 and ZnO in the core-shell nanoheterostructure appear with some enhanced peak intensity. This can be probably caused by the peak overlapping which indicates that the coating process do not change the phase of its components. The two phases in this Figure show that the projection of OH- functional groups outwards of the core material surface could favorably react with Zn^{2+} ions which are usually generated from the decomposition due to heat.

The transmission electron microscopy (TEM) allows determining the morphological properties and the size distributions accurately. Figure 10 displays TEM images obtained by Hong illustrating the deposition and growth of ZnO on the surface instead of a homogeneous nucleation that would produce other particles in the mother solution. In comparison with the morphology of Fe_3O_4, these core-shell heterostructured nanoparticles retain such morphology with a homogeneous growth over the entire surface. Due to the surface treatment of Fe_3O_4, it is expected to obtain a better dispersibility and smaller particle size distribution.

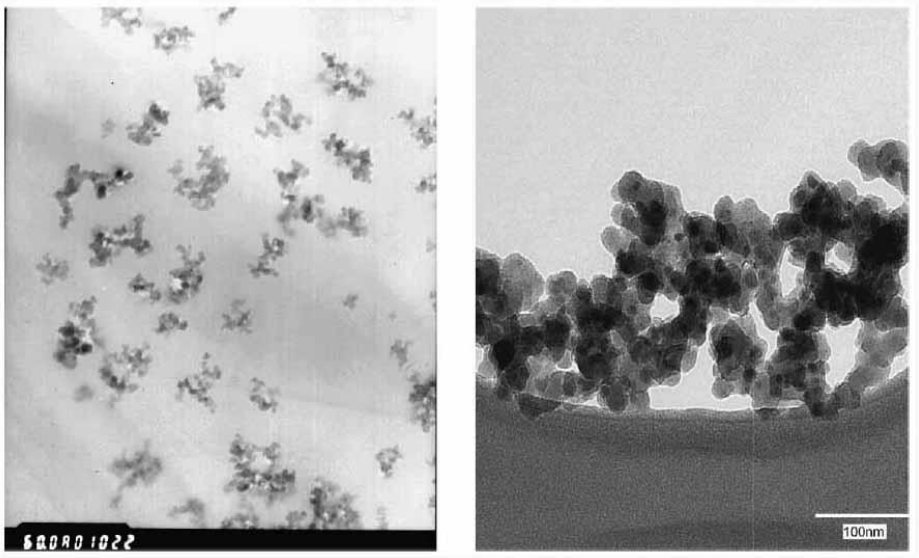

Figure 10: TEM images for Fe_3O_4/ZnO nanoparticles before (left) and after (right) treating the surface [5].

Finally, which type of magnetic response is adopted by this system? It is well-established that bulk magnetite has a superparamagnetic behavior which is distinctive of single-domain nanoparticles and originated from the existence of privileged crystallographic directions along which the electron spins are made parallel most easily. Within the crystal, thermal energy allows total magnetic moment a fast flipping process. Superparamagnetism relaxation may be counteracted by lowering the temperature. This effect is observed at room temperature in particles with sizes smaller than 10 nm [6].

Hong et al found a decrease in saturation magnetization in the Fe_3O_4/ZnO system at room temperature when more ZnO quantity (2→6) (see Figure 11) is added in the process of synthesis. In practice, these nanoparticles can be tested by putting them under the influence of an external applied magnetic field and observing a rapid magnetic response in suspension. From this figure, one could claim that these nanoparticles are superparamagnetic since the values of remanence and coercivity are very small. This decrease in magnetization could be explained by taking into account the diamagnetic contributions of the zinc oxide shell surrounding the magnetic cores but its physical fundamental have not been studied deeply yet.

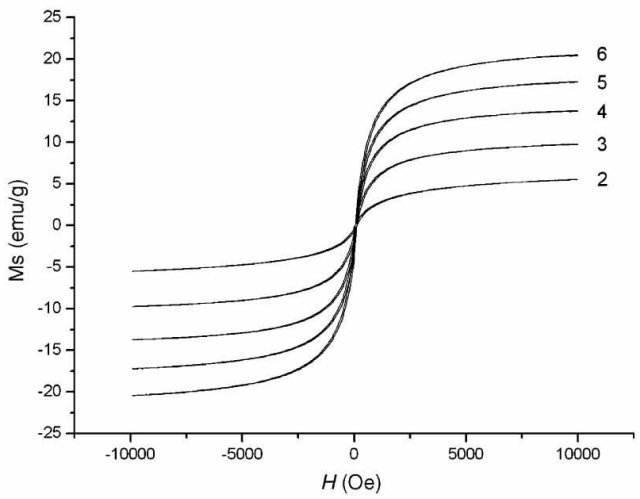

Figure 11: M-H curves at different molar ratios, 2→6 decrease the ZnO quantity in the synthesis process [5].

3.2 Rationale of Fe_3O_4/ZnMnS

Zinc Sulfide (ZnS) is an n-type semiconductor with direct transition and wide band gap (E_g ~ 3.6 eV at 300 K). ZnS possess ~ 40 meV as exciton binding energy and has great advantages such as strong luminescent, environment-friendly, high stability and simple synthesis procedure. It therefore is a good material for shell. In addition, doped-Mn^{2+} ZnS may offer special feature of diluted magnetic semiconductor with consequence in tumor detection and drug targeting [7].

ZnS has cubic structure like Fe_3O_4, thus Fe_3O_4/ ZnS core-shell is suitable for synthesis but for better luminescence it is more advantageous to dope it with paramagnetic Mn^{2+} ions. In this case, the ionic radius for Zn^{2+} is 74 pm (1pm = 10^{-15}m) and for Mn^{2+} is 67 pm allowing Mn^{2+} ions substituting Zn^{2+} ions with no shift in the angular positions obtaining an excellent matching. Thus, ZnMnS system may be a bit stressed, but maintains the cubic structure and Fe_3O_4/ ZnMnS core-shell is feasible.

As it was just worked with the treatment of the magnetite surface, we use HCl to modify its surface interaction and facilitate a better adherence. In earlier work [8], Fe_3O_4/ZnS microspheres evidenced face-centered cubic and hexagonal wurtzite structures, as shown in Figure 12.

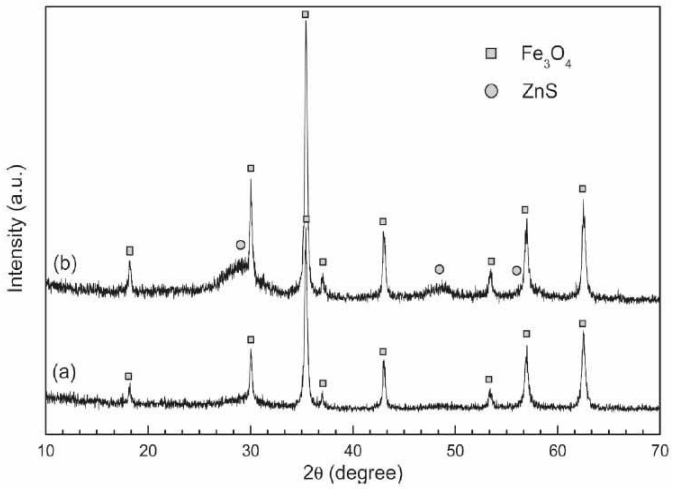

Figure 12: X-ray diffraction patterns for Fe_3O_4 (a) and Fe_3O_4/ZnS microspheres [8].

Similar results were obtained by Wang et al. [9] using a facile synthesis method for superparamagnetic fluorescent hollow nanospheres with the formation of core-shell structure from a homogeneous nucleation as shown in Figure 13. Figure 13-a shows typical shapes of some hollow nanospheres with average diameters ranging between 66 nm and 97 nm.

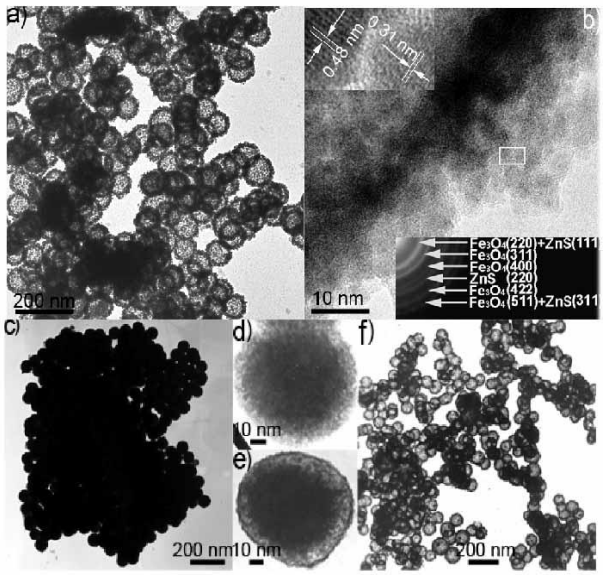

Figure 13: (a) TEM, (b) HRTEM images of Fe_3O_4/ZnS; (c) FeS particles and (d), (e) and (f) subsequent reactions for 2h, 4h and 6h respectively [9].

A more detailed analysis is provided by the high resolution transmission electron microscopy (HRTEM) image (figure 13-b) which reveals that the shell is composed of particles with hexagonallike structures. The other TEM images (figure. 13c-f) show a time-dependent behavior of outer diameter into the formation of these hollow nanospheres. It suggests that Fe_3O_4/ ZnMnS core-shell can be achieved with proper synthesis route.

The most important concern of these Fe_3O_4/ZnMnS core-shell quantum dots is the study of their optical properties, but they will be discussed in the chapter 4. Here we only mentioned that the optical properties of doped-Mn^{2+} ZnS system is still not clear. Although analogous to the bulk behavior, the strong photoluminescence is assigned to the insertion of Mn^{2+} into the ZnS host which generates $^4T_1$-$^6A_1$ localized energetic levels in the forbidden band of the ZnS attributed to crystal field effects [10]. However, in nanocrystals the band gap energies are larger, the lifetimes are shorter and the luminescent efficiency improves. A possible explanation for this phenomenon is directly related to quantum confinement that makes possible the hybridization of the atomic orbitals, s-p states of the ZnS host and the d states of the Mn^{2+} impurity. This favors the radiative recombination against non-radiative one producing the enhanced quantum efficiency.

The physical mechanism of this process for Fe_3O_4/ZnMnS has not been yet completely understood because it is not known how the charge carriers flow towards periphery or a particular direction within material; it is required a molecular and atomic insight. In addition, defect energy levels can also produce photoluminescence and surface of core and ZnS are not smooth enough to assume only vacancy density due to Zn^{2+}.

On the other hand, we know that the magnetic properties of the core material are slightly affected by the insertion of paramagnetic Mn^{2+} ions (low doping concentration) into the host material ZnS since these cores are normally introduced as seeds with a well-defined crystalline structure and the doping occurs in the shell material, i.e., the paramagnetic Mn^{2+} ions substitute to the Zn^{2+} ions but neither to Fe^{2+} nor Fe^{3+} ions. However, the optical properties of the whole system will be remarkably modified. Thus, we can give the magnetic response at room temperature of Fe_3O_4 and Fe_3O_4/ZnS microspheres to clarify the effect to grow bare ZnS layer on the surface of the magnetite (Figure 14). Yu et al found that the saturation magnetization values

were considerably decreased by assembling a thin layer of surrounding diamagnetic ZnS. The difference in saturation magnetization values was almost 33.2 emu g^{-1}. As in the Fe_3O_4/ZnO system, with increasing the thickness of the shell material, this difference tends to rise until a critical value. In spite of the expected diamagnetic contribution of the ZnS, the superparamagnetic trend of the core material was maintained with a considerable drop in saturation magnetization. This can be checked by applying an external magnetic field on the microspheres and observe a fast sedimentation.

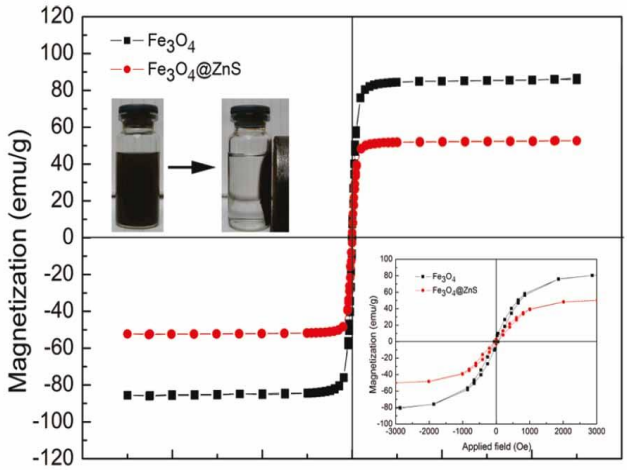

Figure 14: Magnetic responses at 300 K for Fe_3O_4 (black) and Fe_3O_4/ZnS (red) microspheres [9].

Now the main question is to find out at what concentration of paramagnetic Mn ions the superparamagnetic properties of the core are modified or if the unit cell of host material presents some distortion. A plausible answer to this question will be given in the next chapter of this study.

Reference

[1] Ajay Kumar Gupta and Mona Gupta, "Synthesis and surface engineering of iron oxide nanoparticles for biomedical applications", *Biomaterials* (**2005**) 26: 3995-4021.

[**2**] Yu Lu, Yadong Yin, Brian T. Mayers and Younan Xia, "Modifying the surface properties of superparamahnetic iron oxide nanoparticles through a sol-gel approach", *Nanoletters* (**2002**) 2(3): 183-186.

[**3**] Liu B., Wang D., Huang W., Yu M., Yao A., "Fabrication of nanocomposite particles with superparamagnetic and luminescent functionalities" *Materials Research Bulletin* (**2008**) 43:2904-2911.

[**4**] Prachi Joshi, Soumyananda Chakraborti, Pinak Chakrabarti, D. Haranath, Virendra Shanker, Z. A. Ansari, Surinder P. Singh and Vinay Gupta, "Role of Surface adsorbed anionic species in antibacterial activity of ZnO quantum dots against Escherichia coli", *J. Nanosci. Nanotech.* (**2009**) 9: 6427-6433.

[**5**] Hong R. Y., Zhang S. Z., Di G. Q., Li H. Z., Zheng Y., Ding J., Wei D. G., "Preparation characterization and application of Fe_3O_4/ZnO core-shell magnetic nanoparticles" *Materials Research Bulletin* (**2008**) 43:2457-2468.

[6] R. M. Cornell, U. Schertmann, "*The Iron Oxide, Structure, Properties, Reactions, Occurences and Use* " 2nd Edition, WILEY-VCH Verlag GmbH & Co. KGaA, Weinheim, chapter 6, **2003**.

[7] Jian Cao, Jinghai Yang, Yongjun Zhang, Lili Yang, Yaxin Wang, Maobin Wei, Yang Liu, Ming Gao, Xiaoyan Liu, Zhi Xie, "Optimized doping concentration of manganese in zinc sulfide nanoparticles for yellow-orange light emission", *J. Alloys and Compounds* (**2009**) 486: 890-894.

[8] X. Yu, J. Wan, Y. Shan, K. Chen and X. Han, "A facile approach to fabrication of bifunctional magnetic-optical Fe_3O_4/ZnS microspheres" *Chem. Mate.* (**2009**) 21:4892-4898.

[9] Z. Wang, L. Wu, M. Chen, S. Zhou, "Facile synthesis of superparamagnetic fluorescent Fe3O4/ZnS hollow nanospheres" *J. Am. Chem. Soc.* (**2009**) 131:11276-11277.

[10] Wei Chen, Ramaswami Sammynaiken, Yining Huang, Valéry Zwiller, Nicholas A. Kotov, "Crystal field, phonon coupling and emission shift of Mn^{2+} in ZnS:Mn nanoparticles", *J. Appl. Phys.* (**2001**) 89(2): 1120-1129.

Chapter 4: Experimental Details

In this chapter we give a brief summary of the typical route to prepare quantum dots with their respective modifications which were applied to our own synthesis protocol. Furthermore, the more interesting features of our results are presented and discussed.

4.1 Synthesis of the quantum dots

As a large surface to volume ratio implies strong related-surface phenomena, then a high quality preparation technique is required to ensure a minimum quantity of defects on their surface. Such defects trap the photoexcited carriers reducing the quantum efficiency of the quantum dot. Here, we only consider the passivation of these surfaces with assembling an inorganic shell layer. In a typical synthesis process of semiconductor nanocrystals in aqueous solution, the monomers are obtained by heat decomposition of the precursors. The released energy that provokes the nucleation is gained when the monomer concentration achieves to reach the critical oversaturation which lowers the monomer concentration and ensures the growth of the big and small particles from surviving nuclei. Due to monomer exhaustion, the bigger particles start to grow as a result of the dissolution of the smaller ones [1]. In order to acquire an adequate size distribution, the critical parameters such as monomer injection, precursor quantity, growth time, etc., should be suitably controlled.

4.2 Fe_3O_4/ZnO Quantum Dots

4.2.1 Synthesis

Materials

Zinc Nitrate Hexahydrate $Zn(NO_3)_2 \cdot 6H_2$, Iron (II) Chloride Tetrahydrate $FeCl_2 \cdot 4H_2O$, Iron (III) Chloride Hexahydrate $FeCl_3 \cdot 6H_2O$, Sodium Hydroxide NaOH, Sodium Citrate Dihydrate $Na_3C_6H_5O_5 \cdot 2H_2O$, Nitric Acid ACS 70%, Hydrochloric ACS 37%, Ammonium Hydroxide

NH_4OH (14.5 M) were of reagent grade and used without further purification. Acetone and ethanol were of chemical grade, and (high purity) deionized water was used.

Experimental Procedure

The core material Fe_3O_4 was prepared using the route of co-precipitation [2] with minor modifications. First, $FeCl_3.6H_2O$ and $FeCl_2.4H_2O$ were stoichiometrically dissolved, with a molar ratio of 2:1, into deionized water and then an aqueous solution of 0.440 M of NaOH was added. Then controlled vigorous stirring at 100 °C under air for 30 min. was applied to the solution resulting in suspended nanoparticles. The sample was next washed with abundant high purity deionized water and magnetically collected. The as-prepared sample was dried at 60 °C for 24 h (see flow chart in Figure 15).

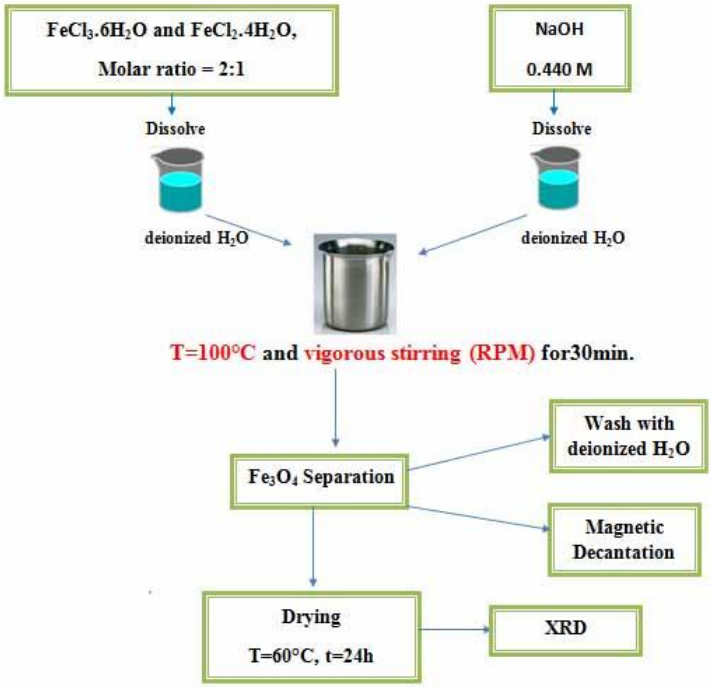

Figure 15: Flow chart for the preparation of magnetite. The red letters represent the parameters that were used to change the size.

Subsequently, the Fe_3O_4 superparamagnetic cores were treated with sodium citrate to avoid any aggregation and provide adsorption sites for Zn species facilitating the formation of the ZnO

shell. As-prepared magnetite sample was dispersed into deionized water and the pH value was regulated to 5.0. Then, $Zn(NO_3)_2$ dissolved in deionized water was slowly dripped into the solution with a molar ratio of magnetite to zinc source adjusted to 1:2. After 1 hour of contact, the pH value was increased up to 9.0 and the temperature was adjusted to 80°C in order to promote the dehydration and atomic rearrangement involved with the formation of ZnO on the surface of magnetite. At the end of the contact stage, the solids were magnetically collected, washed with ethanol and abundant high purity deionized water and dried; see flow chart in Figure 16.

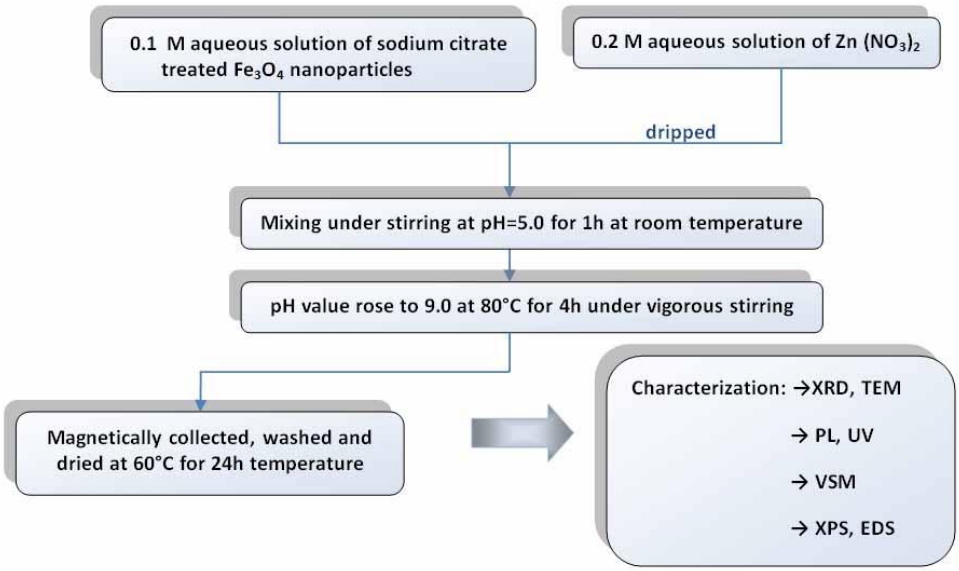

Figure 16: Flow chart for the synthesis of Fe_3O_4/ZnO.

4.2.2 X-Ray Diffraction Measurements

All the X-ray patterns were obtained using a Siemens Diffractometer D5000 (Cu-Kα radiation with λ=0.154315nm). The characteristic peaks attributed to face-centered cubic structure of Fe_3O_4 nanoparticles (core material) according to the standard JCPDF file are shown in Figure 17 which displays six controlled different experiments with almost no impurities included [3]. The three first ones were kept at fixed temperature and the degree of agitation was increased. The three last ones were performed at fixed degree of agitation and the temperature was increased.

The separate experiments were carried out to study the effect of the temperature and the degree of agitation on the particle size during the synthesis process.

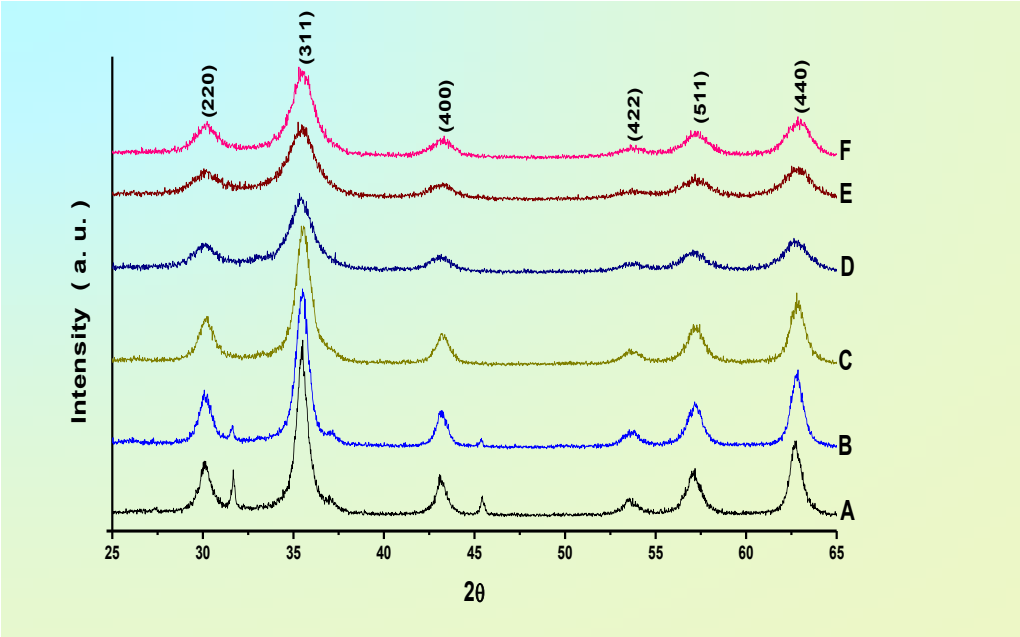

Figure 17: X-ray diffraction patterns for Fe_3O_4 with different synthesis conditions.

The average crystallite sizes of these samples were calculated using the Debye-Scherrer's formula,

$$D_{hkl} = \frac{0.9\,\lambda}{\beta\,cos\theta} \qquad (4.1)$$

where β is the full width at half maximum (FWHM) of the main intense peak (311) in radian, θ is the Bragg angle and λ is the x-ray wavelength. A brief summary of these results are illustrated in Table 1 from where we draw two important observations. First, when the stirring speed increased from 600 to 950 rpm, crystallite size was 12.746 to 8.796 nm. This decrease in the growth kinetics can be plausibly attributed to the anomalous diffusion of particles at higher degree of agitation. In second case, the crystallite size was increased from 6.235 to 8.798 nm (and from 5.762 to 6.379 nm) when the temperature was raised from 25 to 100 °C (and from 50 to 65 °C), see Table 1. This effect suggests that at higher temperature the precipitated particles possess higher crystallinity and larger grain size. An increased temperature promotes the hydrolysis

reaction and the dehydration of ferric chloride precursors, meanwhile a decreased temperature retards to some extent the releases of Fe^{2+} and Fe^{3+} and the formation of magnetite.

Sample	T (°C)	Stir (RPM)	D (nm)
A	100	600	12.476
B	100	900	10.580
C	100	950	8.798
D	25	950	6.235
E	50	1200	5.762
F	65	1200	6.379

Table 1: Variation of the average crystallite sizes for Fe_3O_4 changing the temperature and degree of agitation.

For the assembly of ZnO onto the modified magnetite surface, we performed two batches of experiments in order to show the effect of increasing the amount of shell material in the synthesis process. The former one does not take into account the molar ratios of iron and zinc sources in the synthesis procedure (called sample A), while the latter one does take account of molar ratio (called sample B). If ZnO successfully adhered to the surface and grown in a homogeneous way, one could examine the effect of increasing the shell thickness on their photoluminescence which is related to the exchange coupling interactions. The x-ray diffraction patterns (sample A) of the as-prepared samples showed the development of isolated and joint crystalline phases of cubic Fe_3O_4 [4] and hexagonal ZnO wurtzite [5], see Figure 18. From the broadness of the diffraction peaks the formation of nanosize phases can be used and the use of Debye-Scherrer's equation yielded a value of 17.335 nm for the average crystallite size taking the (440) peak as reference. The deposition and growth of a ZnO layer on the core material surface can be deduced from the figure 18-c. It can be observed that several enhanced peak intensities could be caused by the peak overlapping which suggests that the coating process did not change the individual phases.

With the aim of making sure us whether the surface treatment modified the structure of magnetite or not, we did similar structural measurements before and after such modification.

Figure 19 demonstrates that this treatment with sodium citrate did not change the crystalline structure of Fe_3O_4 through these experiments since the characteristic peaks attributed to cubic structure did not presented any angular shift. Finally, it is worth mentioning that lattice parameters of maghemite (γ-Fe_2O_3) are quite like to those of Fe_3O_4 but the major peak number is greater in Fe_2O_3 than in that of Fe_3O_4. Thus, the peaks that appear in Figure 19 belong indisputably to the Fe_3O_4 rather than the Fe_2O_3.

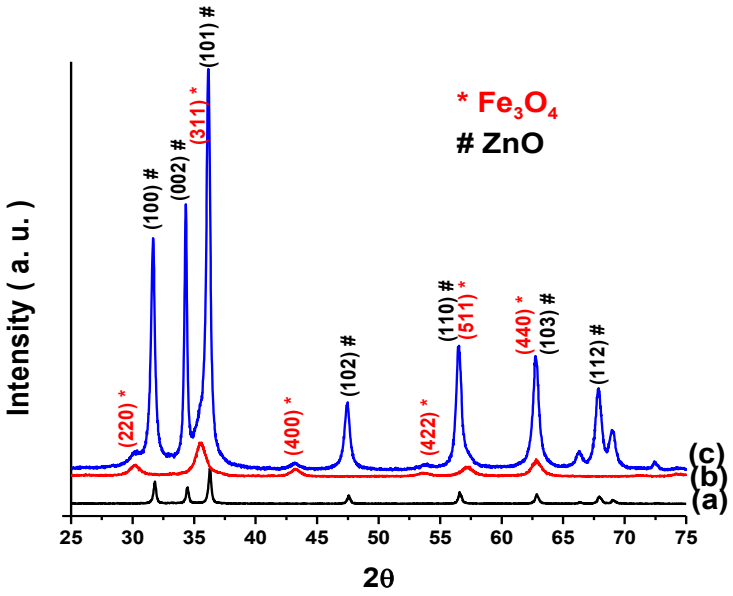

Figure 18: X-ray diffraction spectra for ZnO (a), Fe_3O_4 (b) and Fe_3O_4/ZnO (c).

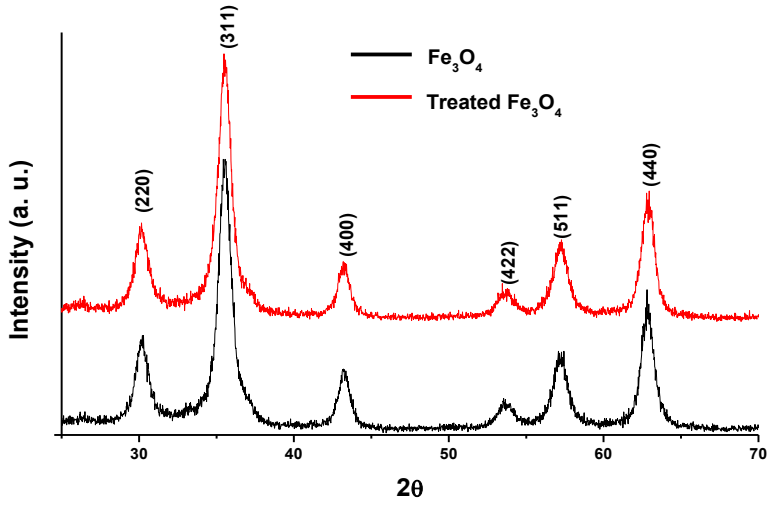

Figure 19: X-ray diffraction patterns for Fe_3O_4 before and after treatment showing none change through the modification with sodium citrate.

On the other hand, the diffraction peaks of sample B did not show any angular displacement of the peaks and the intensities of their peaks did not vary enough to be considered. For that reason, their graphics are not presented in this work but the effect that they have on the optical and magnetic properties will be discussed later.

4.2.3 TEM Measurements

The TEM images for the Fe_3O_4/ZnO particles with a molar ratio of 1:2 are shown in the figure 20. These images were obtained using a conventional carl zeiss LEO 922 energy filtered TEM. The photographs display that Fe_3O_4/ZnO particles ranged from 13 to 18 nm in diameter as shown in Table 2. Using the equation 4.1 we obtained a value of 14.603 nm compared with 15 nm (see Figure 21).

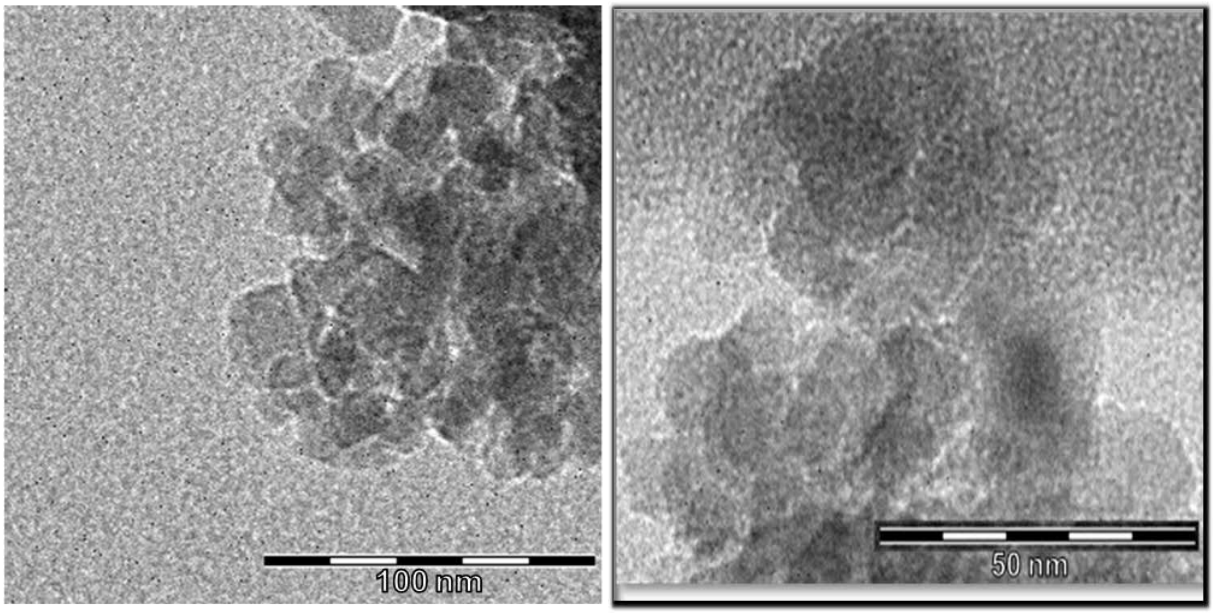

Figure 20: TEM figures for the Fe_3O_4/ZnO particles with R=1:2 corroborating the size at nanoscale. The contrast in core and shell images verifies the core-shell structure.

Likewise, the calculation for the average crystallite size of core material (9.424nm) was smaller than this value and as did not show any change in diffraction patterns for treated core material, it is possible to affirm that this treatment with sodium citrate provides the Fe_3O_4 nanoparticles with larger specific surface area and surface energy. As a result, the ZnO precursor can deposit on the

surface of the core material to form the core-shell heterostructure as proven in the two photographs.

In thermodynamic terms, this behavior is a spontaneous process to reduce the overall free energy, that is, the increase in the particle size reduces remarkably the specific surface area and surface energy of the nanoparticles. Thus, the surface modification of Fe_3O_4 clearly affects the surface coating process.

Sample	**Molar Ratio**	**D_{440} (nm)**	**Thickness (nm)**
Fe_3O_4	-	9.424	-
Fe_3O_4/ZnO	1:2	14.603	2.589
Fe_3O_4/ZnO	1:3	15.107	2.841
Fe_3O_4/ZnO	1:5	15.788	3.182

Table 2: Variation of average crystallite size and their respective shell thicknesses for Fe_3O_4/ZnO as the molar ratios are increased.

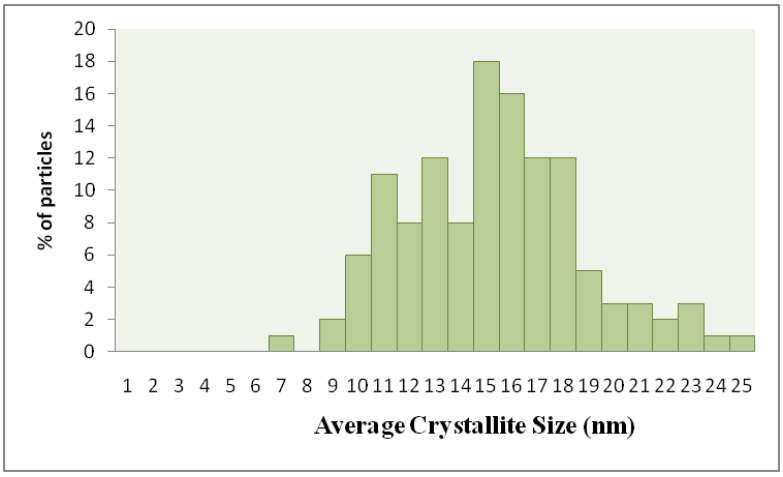

Figure 21: Size distribution for the particles of Fe_3O_4/ZnO. It can be observed that occurrence maximum peak is just at 15 nm as approximately calculated with the eq. 4.1 (see Table 2).

4.2.4 UV and PL Measurements

A UV-vis spectrophotometer (DU 800, Beckman Coulter) was used to study the optical absorption and a spectrofluorometer FluoroMax-2 at room temperature with a 150mW continuous ozone-free Xe lamp to investigate the luminescent properties. The optical absorption spectra for ZnO and Fe_3O_4/ZnO nanoparticles of the sample A are shown in the figure 22 with an absorption peak at 351 nm for ZnO and at 361 nm for Fe_3O_4/ZnO. The band broadening for the absorption of Fe_3O_4/ ZnO nanoparticles suspended in ethanol suggests a narrower distribution of the nanocrystal size than the ZnO nanoparticles, see Figure 21. One can also observe a slight redshift in the excitonic peak which is attributed to the decrease in quantum confinement due to "crystal growth" which is generated by the growth of a ZnO layer on the treated magnetite surface (core material).

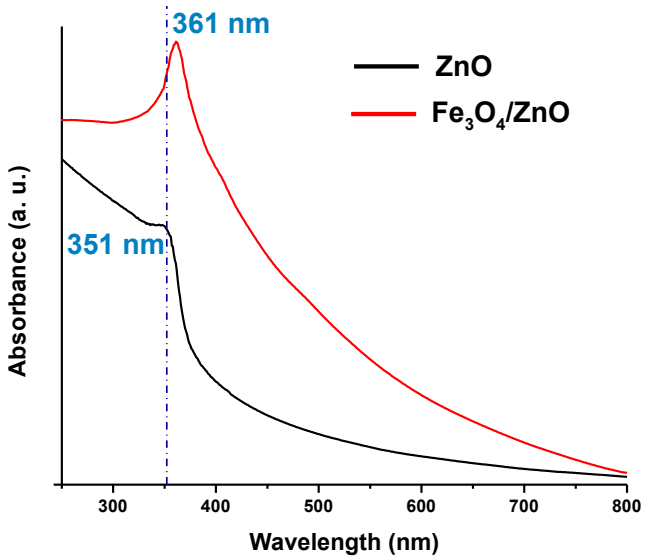

Figure 22: Optical absorption spectra for ZnO (black) and Fe_3O_4/ZnO (red).

The same effect is observed in the figure 23 for the measurements on sample B with an optical absorption peak at 351 nm for ZnO, at 358 nm for Fe_3O_4/ZnO (R=1:2), at 363 nm for Fe_3O_4/ZnO (R=1:3) and at 364 nm for Fe_3O_4/ZnO (R=1:5). Thus, it is presumed that when the molar ratio of iron to zinc source increased, more ZnO is deposited on the core material surface. Figure 24 shows the emission peaks of measurements of the sample B; these figures were constructed under excitation of 250 and 350 nm for questions of visualization. Figure 24-(a) displays the

peak of near-band edge UV emission at 367 nm and the band of broad defect-related visible emission at ~540 nm [6] at room temperature.

This luminescent emission is still controversial in spite of the numerous studies carried out. In this work, we suppose that its origin is attributed to oxygen vacancy on the surface highlighting the fact that the spectral position and the intensity of the visible emission also depend on the fabrication process. The figure 24-(b-d) shows the UV and visible emission peaks at room temperature becoming stronger with increasing ZnO content.

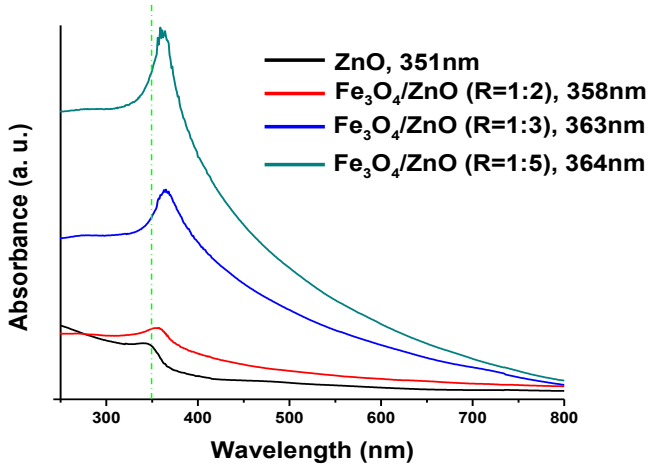

Figure 23: Absorption spectra for Fe_3O_4/ZnO at different molar ratio in comparison to pure ZnO.

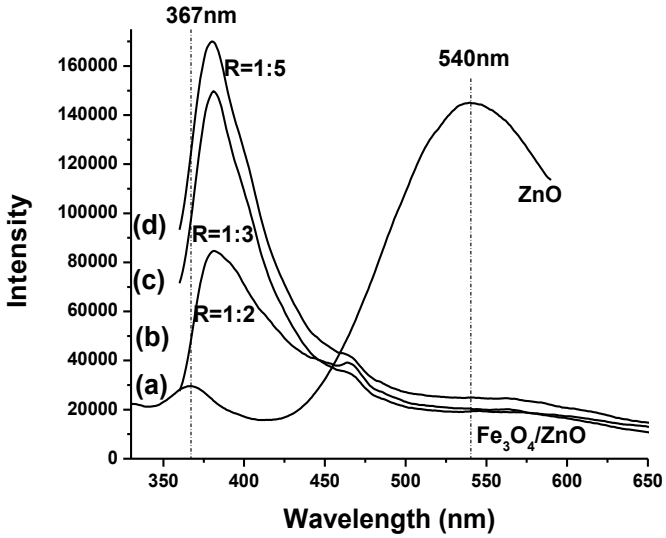

Figure 24: Photoluminescence spectra for ZnO (a) and R=1:2 (b), R=1:3(c) and R=1:5(d) Fe_3O_4/ZnO nanoparticles.

The luminescence quenching can be attributed to the interfacial charge transfer between Fe_3O_4 nanoparticles and ZnO nanocrystals. The figure 25 reveals a strong excitonic emission peak at 380 nm and very weak related-defect emission band at ~ 568 nm suggesting the rearrangement of electronic configuration in those core-shell structures. This result is amazing since as far as it is known the pure Fe_3O_4 nanoparticles do not exhibit any kind of luminescence.

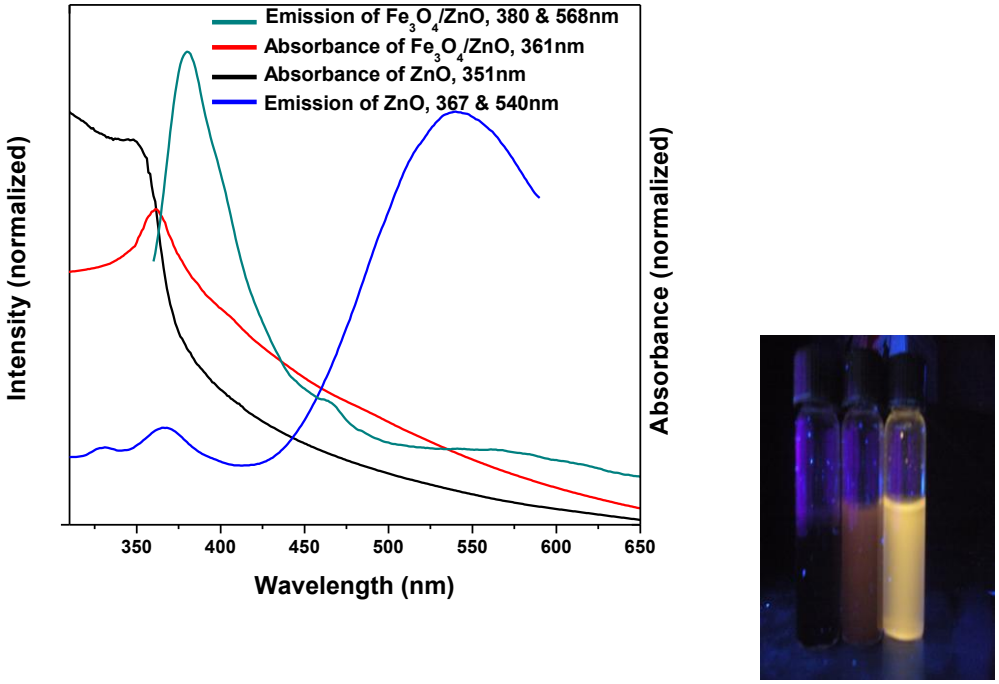

Figure 25: Optical absorption and photoluminescence spectra for pure ZnO and Fe_3O_4/ZnO (left) and photographs obtained by exposing a UV lamp on the samples: Fe_3O_4 (black), Fe_3O_4/ZnO (brown) and ZnO (yellow).

According to the framework of spatial confinement of electron and hole wavefunctions, the carriers migrate towards the core material to avoid the interaction with the trap states on the surface tuning their overlapping with magnetic core. This will likely give rise to the reduction in band gap according to the tight binding model [7]. This effect can be seen in Figure 25 in the form of red shift in the excitonic emission of ZnO from 367 to 380 nm.

4.2.5 VSM Measurements

The magnetic properties were measured at room temperature with a vibrating sample magnetometer (VSM, Lakeshore 7400). The magnetic response to an external applied magnetic field for the A sample is presented in the figure 26. These M-H curves at room temperature indicate a saturation magnetization of 59.87 emu/g for the pure Fe_3O_4 nanoparticles and 15.64 emu/g for the as-synthesized Fe_3O_4/ZnO nanoparticles with no coercivity nor remanence due to its very small size. This decrease in magnetization can be attributed to the presence of the diamagnetic zinc oxide layer that surrounds the superparamagnetic cores.

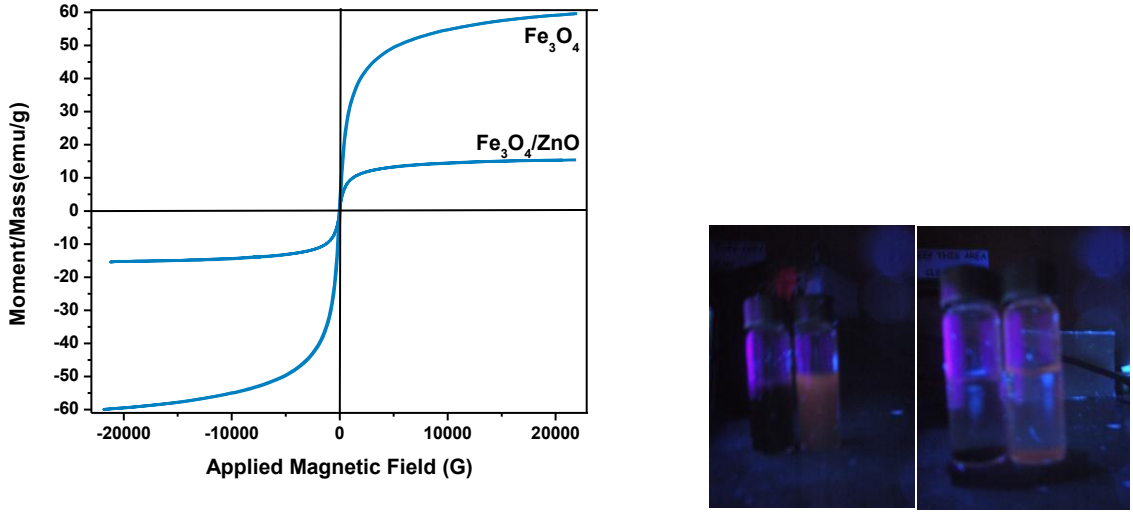

Figure 26: M-H curves for Fe_3O_4 (59.87 emu/g) and Fe_3O_4/ZnO (15.64 emu/g) nanoparticles (left) and photographs of the samples obtained by a UV lamp and a permanent magnet: Fe_3O_4 (black) and Fe_3O_4/ZnO (brown).

Figure 27 (sample B) shows that with the increase of the diamagnetic ZnO thickness on the superparamagnetic cores, the saturation magnetizations decreased considerably. The pure Fe_3O_4 nanoparticles presented a 57.17 emu/g saturation magnetization and the Fe_3O_4/ZnO nanoparticles decreased at 15.01, 9.63 and 7.72 emu/g for R=1:2; 1:3 and 1:5 respectively suggesting that this behavior can be modulated by varying the molar ratios of iron to zinc sources.

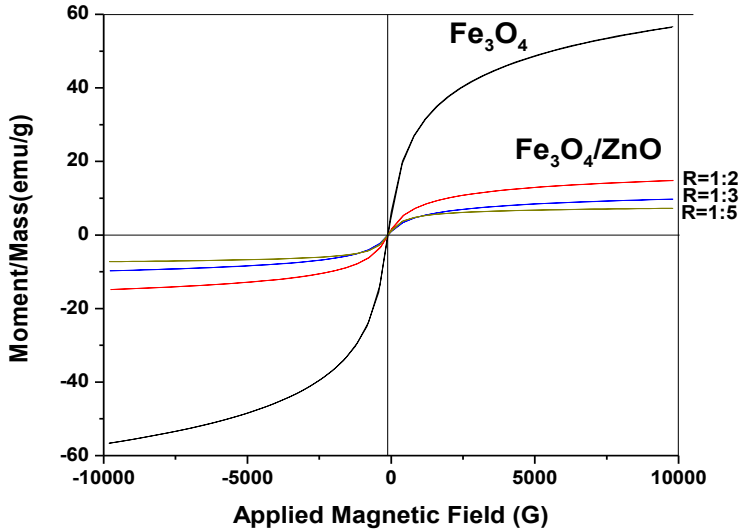

Figure 27: M-H curves for Fe_3O_4 and R=1:2, R=1:3 and R=1:5 Fe_3O_4/ZnO nanoparticles at different molar ratios.

4.2.6 XPS Measurements

In order to know if the ZnO was deposited on the magnetite, the XPS elemental analysis for Fe_3O_4/ZnO core-shell nanoparticles was carried out using a PHI 5600 Multisystem, equipped with an Al source and a neutralizer at a base pressure of $5x10^{-10}$ torr. The two characteristic peaks of ZnO with binding energies are located in 1046 eV for Zn $2p^{1/2}$ and in 1023.37 eV for Zn $2p^{3/2}$ with an overall atomic concentration of 31.43 which demonstrate the presence of Zn on the surface of the magnetic seed at this shell thickness, see Figure 28. In addition, it can also be observed the peaks corresponding to the iron oxide with binding energies of 725.94 eV for Fe $2p^{1/2}$ and 711.97 eV for Fe $2p^{3/2}$ with an overall atomic concentration of 9.98 which suggest two situations. The first situation is that no all the nanocores were successfully and completely coated by ZnO layers, i.e., maybe there was several spaces free of ZnO. The second situation is that the incident photoelectrons were powerful enough to penetrate the core of nanosystem. The first one is the most reasonable. On the other hand, the peaks corresponding to O 1s (531.82 eV) and C 1s (286.09 eV) are shown as reference.

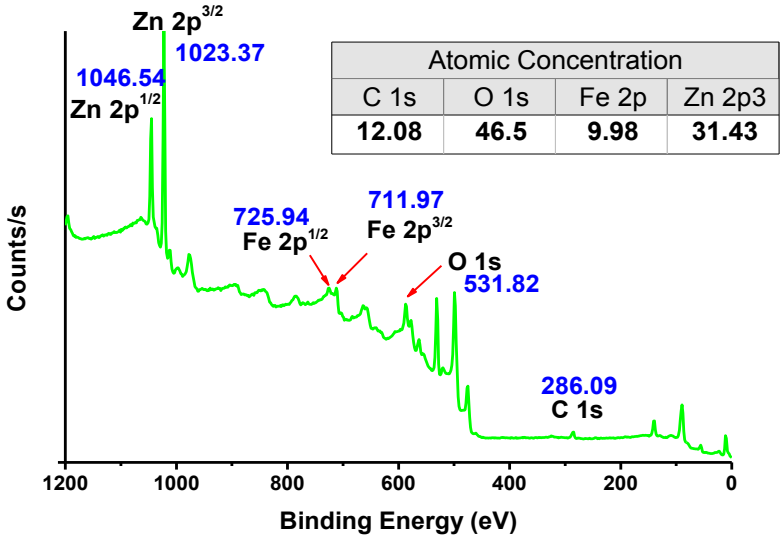

Figure 28: Surface chemistry of Fe_3O_4/ZnO nanoparticles obtained by x-ray photoelectron spectroscopy suggesting the presence of Zn on the surface of core material.

This research was published in *Nanotech* (**2010**) 3: 405-408.

4.3 Fe_3O_4/ZnMnS Quantum Dots

4.3.1 Synthesis

Materials

Zinc Sulfate Monohydrate $ZnSO_4 \cdot H_2O$ (99.9%), Manganese (II) Sulfate Monohydrate $MnSO_4$ (98%+), Hydrochloric Acid, for analysis, ca. 37% solution in water, Sodium Sulfide Na_2S were of reagent grade and used without further purification. Acetone and ethanol were of chemical grade, and (high purity) deionized water was used.

Experimental Procedure

First, the superparamagnetic Fe_3O_4 nanoparticles were treated with HCl 0.05M under ultrasonication for 30 min. then dispersed into high purity deionized water. An aqueous solution of $ZnSO_4$ (0.2 M) with different concentrations of $MnSO_4$ dopant was added to the first solution

under vigorous stirring for 2h at room temperature. After it was dripped an aqueous solution of Na_2S (0.2 M) and put next under vigorous stirring for 6h at room temperature. Finally, magnetically collected, washed with abundant water and ethanol and dried at 80°C for 24h, see flow chart in Figure 29.

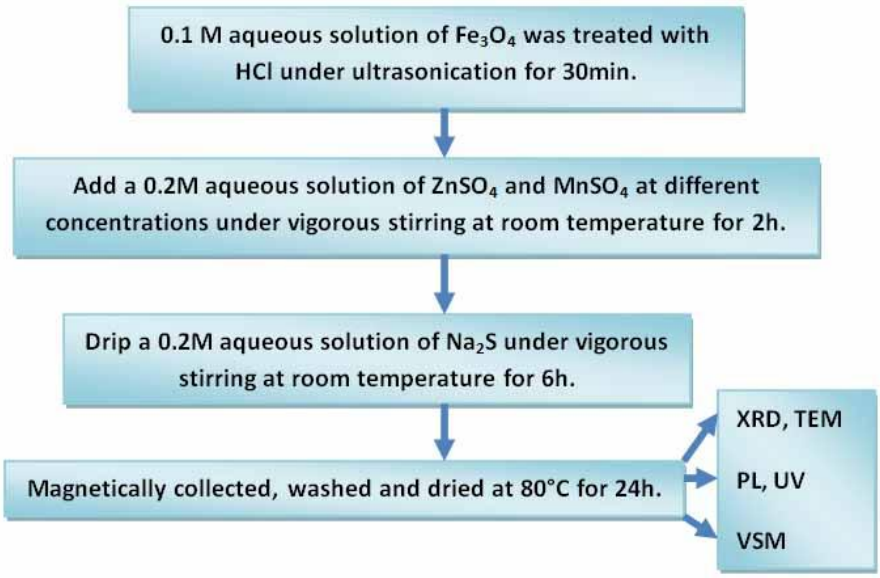

Figure 29: Flow chart for the preparation of Fe_3O_4/ZnMnS.

4.3.2 XRD Measurements

The diffraction peaks corresponding to Fe_3O_4 and ZnS isolated phases and doped-Mn^{2+} Fe_3O_4/ZnS (20 and 25 percentages of dopant species) combined phases are shown in Figure 30. These concentrations were put to evidence that at smaller concentrations we did not find any luminescent peak belonging to the Mn^{2+} paramagnetic ion. All peak broadenings suggest that these phases as isolated as combined present sizes at nanoscale. The isolated characteristic peaks attributed to face-centered cubic structure of Fe_3O_4 and the cubic ZnS phase nanoparticles according to the standard JCPDF [8] are also verified in this Figure. From the peaks of the core-shell system can be deduced that, in fact, there was a development of both phases at nanoscale. Additionally, it can be observed a good substitution between paramagnetic Mn^{2+} (ionic radii 67 pm) ion and Zn^{2+} (74 pm) ion which did not modify the unit cell of host material. The structural matching of the core and shell materials were guaranteed due to that both materials possess cubic

structure in contrast with the cubic structure of magnetite and hexagonal structure of ZnO for the first core-shell system. Using the eq. 4.1 and taking the main peak (311) of pure magnetite, it was found an average crystallite size of 8.710 nm and in the same peak for Fe_3O_4/ZnS at x=0.25 was found an average crystallite size of 13.455 nm which implies a shell thickness of doped-Mn^{2+} ZnS of ~2.3 nm.

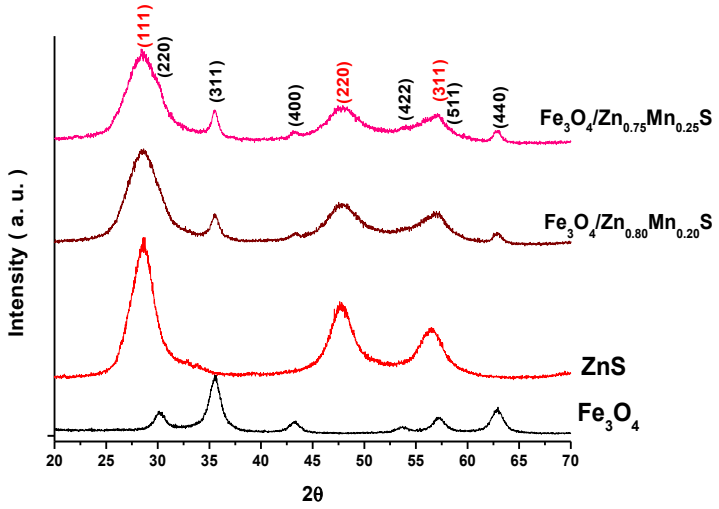

Figure 30: X-ray diffraction patterns showing the formation of both Fe_3O_4 and ZnS phases in the $Fe_3O_4/Zn_{1-x}Mn_xS$ core-shell heterostrucutures with x=0.20 and x=0.25.

4.3.3 TEM Measurements

The TEM photographs demonstrated a successfully deposition of shell material onto the treated-HCl surface of the core material and an oval shape that was acquired from the core material, see Figure 31. The photographs display that Fe_3O_4/ZnMnS particles were 10-18 nm in diameter corroborating their nature at nanoscale. Using the eq. 4.1 was obtained a value of 13.455 nm compared with 14 nm (see Figure 32). In this case, it is also possible to affirm that this treatment with HCl provides the Fe_3O_4 nanoparticles with larger specific surface areas. Thus, ZnMnS can be deposit on the surface of the core material to form the core-shell heterostructure as proven in the two photographs.

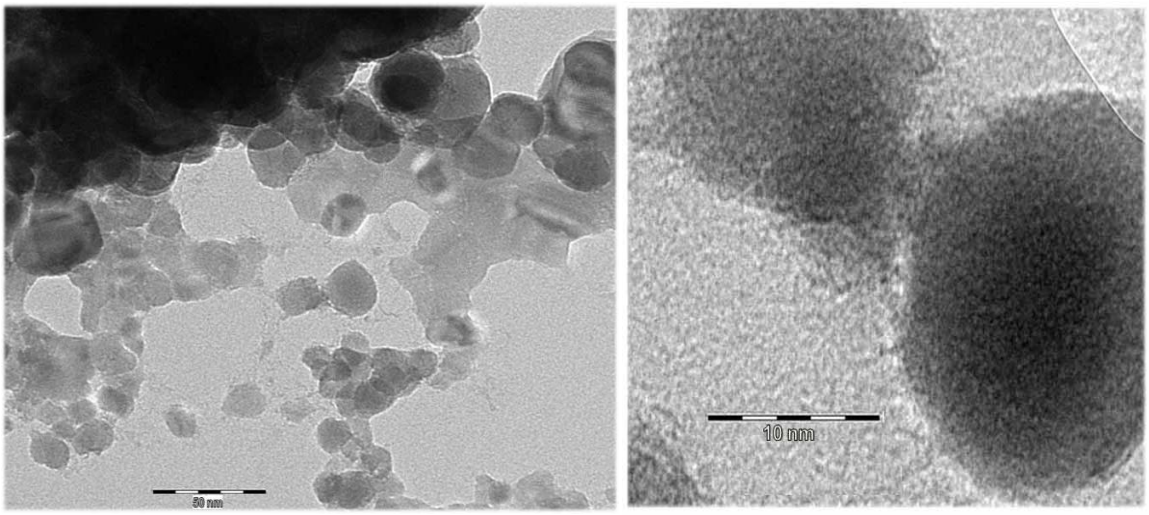

Figure 31: TEM images for Fe_3O_4/ZnMnS at magnifications of 50 and 10 nm. The contrast in core and shell images verifies the core-shell structure.

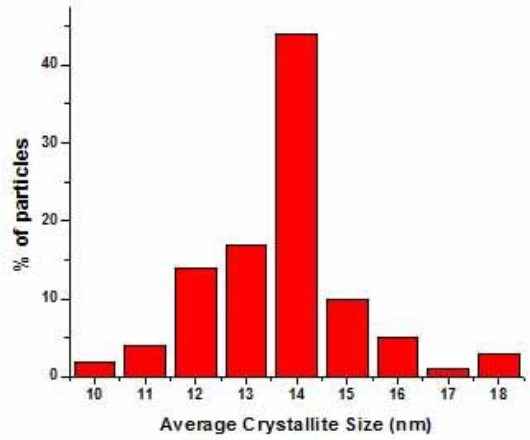

Figure 32: Size distribution for the particles of Fe_3O_4/ZnMnS. It can be observed that occurrence maximum peak is just at 14 nm as approximately calculated from XRD measurements.

4.3.4 PL Measurements

Figure 33 shows the emission spectra at room temperature for pure ZnS, doped-Mn^{2+} (x=0.10, higher concentrations modified the unit cell of the host material) ZnS and doped-Mn^{2+} Fe_3O_4/ZnS at x=0.20 and x=0.25. The pure ZnS presents an emission band centered at ~396 nm when excited by 250 nm which can be attributed to the defect-state recombination presented

mostly on the surface of the nanocrystal [9]. The doped-Mn^{2+} ZnS at x=0.10 exhibits an additional strong orange emission peak around 598 nm which could be ascribed to the well-known $^4T_1$-$^6A_1$ Mn $d-d$ transition of Mn^{2+} ions suggesting a strong coupling between the Mn d levels and host states [10]. It is well-established that Fe_3O_4 nanoparticles do not show signs of any emission peak in the interest region but amusingly, the doped-Mn^{2+} Fe_3O_4/ZnS core-shell heterostructured nanoparticles with different atomic concentrations of dopant species exhibited a weak and broad emission peak centered at 605 nm (see Figure 34) which indicates that the growth of a doped-Mn^{2+} ZnS layer on the surface of core material was successfully done.

.

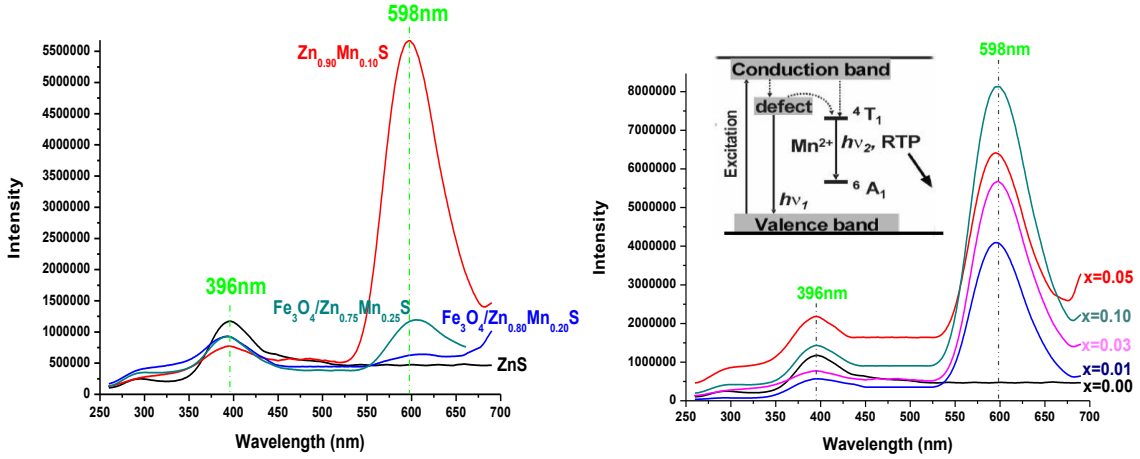

Figure 33: Photoluminescence spectra for $Fe_3O_4/Zn_{1-x}Mn_xS$ (x=0.20, 0.25) compared with bare and doped-Mn^{2+} (x=0.10) ZnS (left). Strong emission peaks for doped ZnS at different concentrations with an inset indicating the dopant energetic level (right).

This additional emission peak also indicates the actual incorporation of dopant species into host ZnS structure. As mentioned, the slight redshift can be assigned to the effects of quantum confinement since a layer of shell material was developed on the core material, thus making system grow. The photoluminescence quenching is obviously evidenced from the figure 33 which is possibly ascribed to interfacial charge transfer between Fe_3O_4 nanoparticles and doped-ZnS nanocrystals.

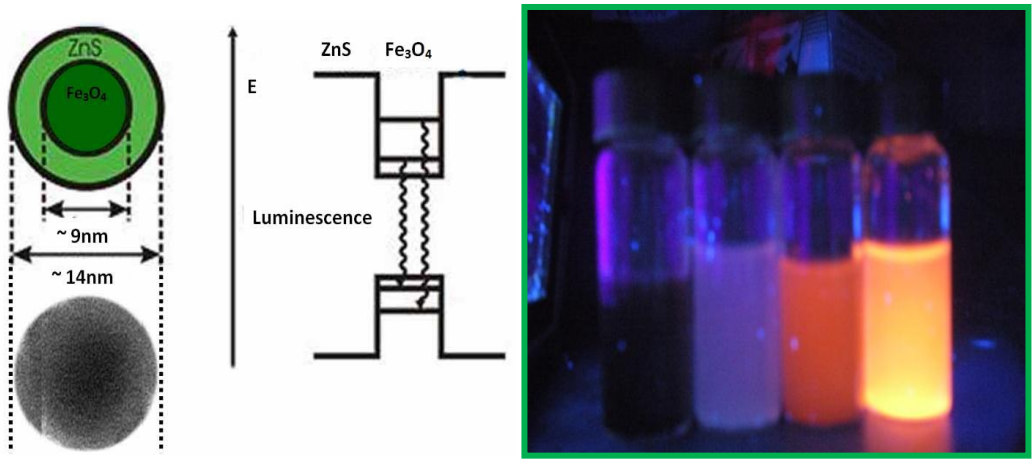

Figure 34: Schematics for the band structure of Fe_3O_4/ZnS with real sizes (left) and photographs of the samples obtained by a UV lamp: Fe_3O_4 (black), ZnS (gray), $Fe_3O_4/Zn_{0.75}Mn_{0.25}S$ (orange) and $Zn_{0.90}Mn_{0.10}S$ (ligh orange).

4.3.5 VSM Measurements

The magnetic response to an external applied magnetic field at room temperature of pure Fe_3O_4 and doped-Mn^{2+} Fe_3O_4/ZnS at 25% is presented in the figure 35. These M-H curves indicated a saturation magnetization of 42.29 emu/g for the pure Fe_3O_4 nanoparticles and 5.21 emu/g for the as-synthesized doped-Mn^{2+} Fe_3O_4/ZnS nanoparticles. It was not observed any coercivity or remanence since the magnetic domain of the nanoparticles was kept very tiny [8]. At room temperature, the pure Fe_3O_4 nanoparticles present a superparamagnetic behavior and the pure ZnS nanoparticles exhibit a diamagnetic behavior, then by assembling the core-shell system of these materials we have to expect an appreciable decrease in magnetization which is basically assigned to the presence of the diamagnetic zinc sulfide layer that surrounds the superparamagnetic cores. But very surprisingly, by doping the shell material with paramagnetic Mn^{2+} ions at 25%, a slight ferromagnetic behavior at room temperature is appeared (see the inset from Figure 35). Observed ferromagnetism could be assigned to exchange mechanism between 3d electrons in the partially occupied 3d-orbitals of the Mn^{2+} ions and the magnetite nanocrystals. Although a quite weak coercivity was found, ferromagnetic behavior can be suggested for this composition. Finally, it is possible to say that this effect depends greatly on the type (magnetic behavior) and concentration of dopant species.

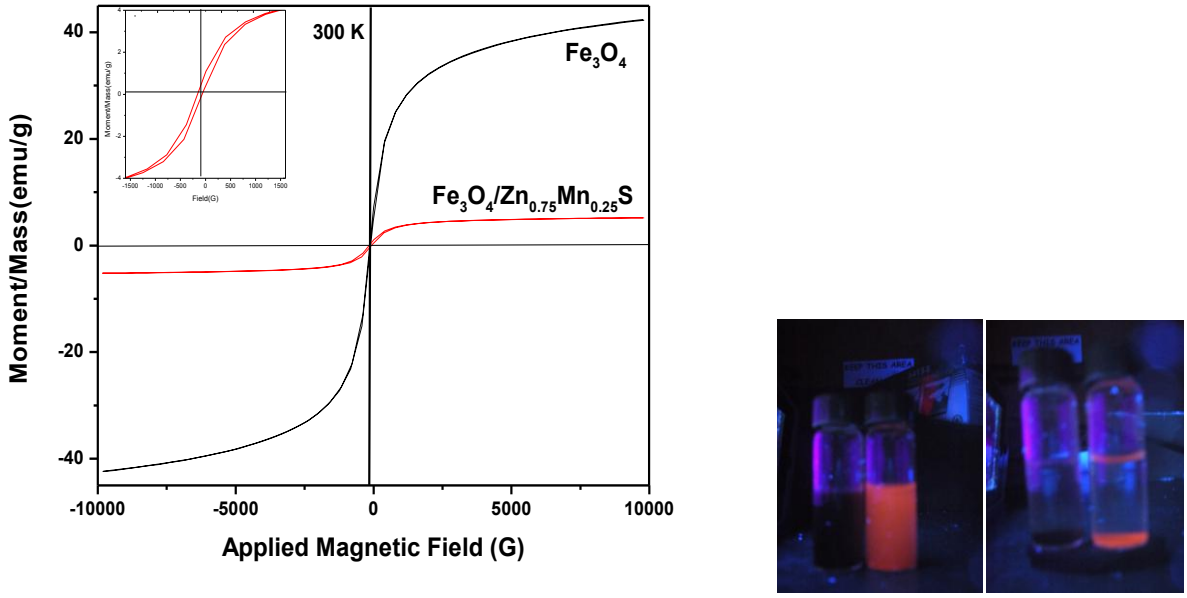

Figure 35: M-H curves for Fe_3O_4 (42.29 emu/g) and $Fe_3O_4/Zn_{1-x}Mn_xS$ with x=0.25 (5.21 emu/g). The inset shows the magnification of the same figure around the origin suggesting a slightly ferromagnetic behavior at room temperature (left) and photographs of the samples obtained by a UV lamp and a permanent magnet: Fe_3O_4 (black) and $Fe_3O_4/Zn_{0.75}Mn_{0.25}S$ (orange).

Reference

[1] Andrey L. Rogach, "*Semiconductor nanocrystal quantum dots: synthesis, assembly, spectroscopy and applications*", Sprunger Wien New York, chapter 1, **2008**.

[2] Hua C. C., Zakaria S., Farahiyan R., Khong L. T., Nguyen K. L., Abdullah M., Ahmad S., "Size-controlled synthesis and characterization of Fe3O4 nanoparticles by chemical coprecipitation method" *Sains Malaysiana* (**2008**) 37(4): 389-94.

[3] Shouheng Sun and Hao Zeng, "Size controlled synthesis of magnetite nanoparticles" *J. Am. Chem. Soc.* (**2002**) 124:8204-8205.

[4] Liu B., Wang D., Huang W., Yu M., Yao A., "Fabrication of nanocomposite particles with superparamagnetic and luminescent functionalities" *Materials Research Bulletin* (**2008**) 43:2904-2911.

[5] L. Spanhel, M. Anderson, "Semiconductor clusters in the sol-gel process, quantized aggregation, gelation and crystal growth in concentrated zinc oxide colloids" *J. Am. Chem. Soc*. (**1991**)113:2826-2833.

[6] A. van Dijken, E. A. Meulenkamp, D. Vanmaekelbergh, A. Meijerink, "The luminescence of nanocrystalline ZnO particles, the mechanism of the ultraviolet and visible emission" *Journal of Luminescence* (**2000**) 87-89, 454-456.

[7] Bussian D., Crooker S., Yin M., Brynda M., Efros A., Klimov V., "Tunable magnetic exchange interactions in manganese-doped inverted core-shell ZnSe-CdSe nanocrystals" *Nature Mater.* (**2009**) 8**:** 35-40.

[8] X. Yu, J. Wan, Y. Shan, K. Chen and X. Han, "A facile approach to fabrication of bifunctional magnetic-optical Fe_3O_4/ZnS microspheres" *Chem. Mate.* (**2009**) 21:4892-4898.

[9] R.N. Bhargava and D. Gallagher, "Optical properties of manganese-doped nanocrystals of ZnS", *Phys. Rev. Lett.* (**1994**) 72(3): 416-19.

[10] Hao-Ying Lu, Sheng-Yuan Chu, Soon-Seng Tan, "The characteristics of low-temperature-synthesis ZnS and ZnO nanoparticles" *Journal of Crystal Growth* (**2004**) 269: 385-391.

Chapter 5: Conclusions

5.1 Findings of the Present Work and Comparison with Other Works

This systematic research was motivated by the need to assembly core-shell heterostructured nanoparticles for applications in photodynamic therapy. Our main purpose was to figure out the effect of depositing and growing a layer of ZnO and ZnMnS on the previously treated superparamagnetic Fe_3O_4 nanoparticle surface. We have successfully obtained nanoparticles with well-defined structural and morphological properties which showed a good superparamagneto-luminescent behavior. In short, from the study presented and discussed here, it is concluded that:

Fe_3O_4/ZnO System

- The synthesis of the Fe_3O_4/ZnO core-shell heterostructured nanoparticles can be successfully attained from a low cost, nontoxic and aqueous route at room temperature without need of using very sophisticated equipments.
- The deposition of ZnO on the surface of the core material can be achieved by modifying the magnetite surface since the structural mismatching with the ZnO would create more traps for photocarriers reducing dramatically the radiative recombination.

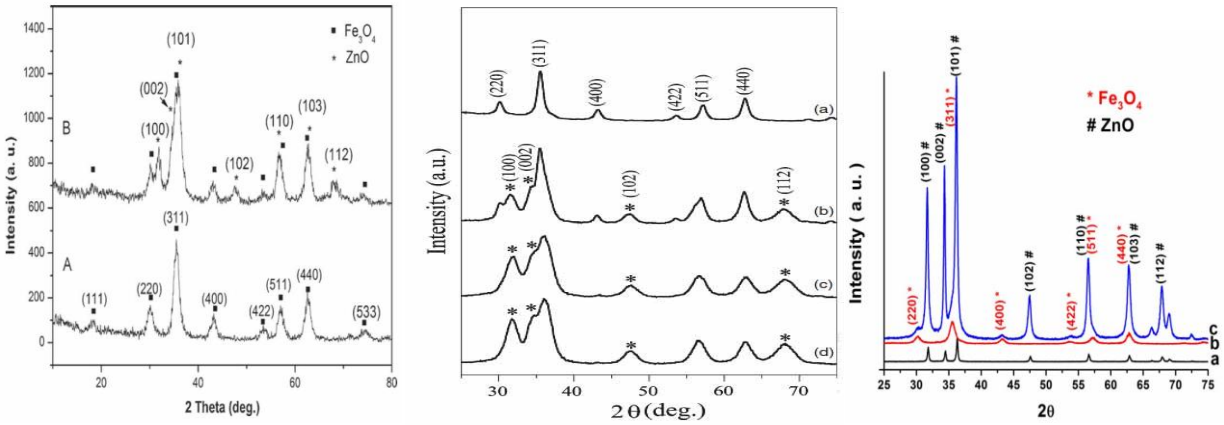

Figure 36: A comparison of x-ray diffraction patterns for Fe_3O_4/ZnO of others and our work, from left to right: Wan et al. [1] with A: Fe_3O_4 and B: Fe_3O_4/ZnO; Zou et al. [2] with (a): Fe_3O_4 and (b), (c) and (d): Fe_3O_4/ZnO at increasing molar ratios; and present work with (a): ZnO, (b) Fe_3O_4 and (c) Fe_3O_4/ZnO.

This treatment also facilitated the adherence of layers of shell material taking advantage of the electrostatic interaction at the interface. The tendency of the Fe_3O_4 nanoparticles to be aggregated into clusters reduces the superparamagnetic behavior; however, by using this treatment we accomplished these nanoparticles to be monodispersed. In addition, according to the structural and morphological tests, the development of the combined Fe_3O_4 and ZnO phases presented a good matching in comparison to the diffraction peaks of isolates phases. Finally, we conclude that the surface treatment with sodium citrate did not alter the unit cell of Fe_3O_4 as evidenced from the XRD patterns, see Figure 36 for comparison with other works.

- Despite pure Fe_3O_4 nanoparticles did not show any emission peak, the Fe_3O_4/ZnO nanoparticles exhibited strong emission peaks which can be shifted by varying the thickness of shell material. This effect was obtained with unique properties that present the materials at nanoscale (quantum confinement).
- The considerable drop in the saturation magnetization due to the diamagnetic layer grown on the core material can be modified by increasing the shell thickness. An increase in shell thickness corresponded to a stronger drop in saturation magnetization, see Figure37.

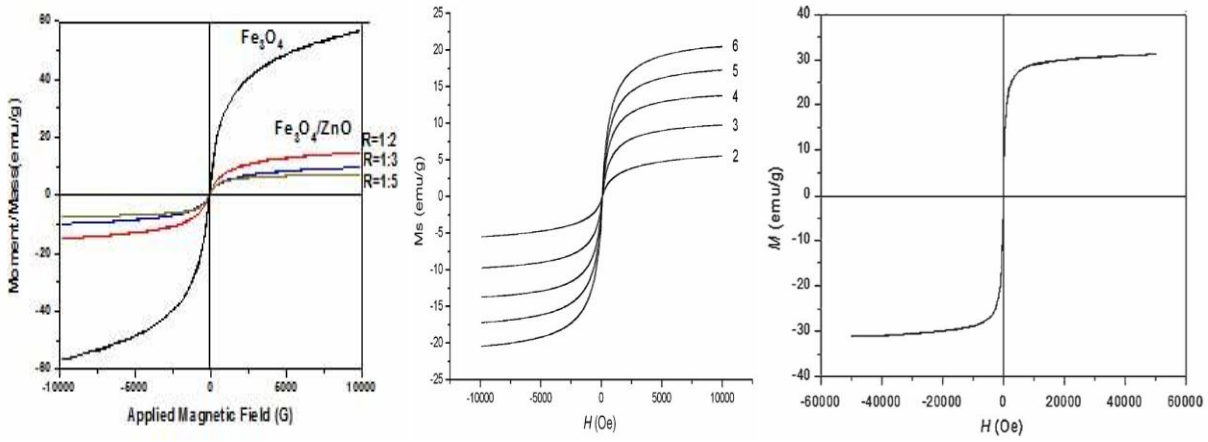

Figure 37: A comparison of M-H curves at room temperature for Fe_3O_4/ZnO of others and our work, from right to left: Wan et al. [1] with 31.25 emu/g; Hong et al. [3] with (6): 20.33, (5): 17.12, (4): 13.67, (3): 9.72 and (2): 5.52 emu/g at increasing molar ratios; and present work with 15.01, 9.63 and 7.72 emu/g at R=1:2; 1:3 and 1:5 respectively.

- The presence of zinc at high atomic concentration on the surface of Fe_3O_4 provided by elemental composition analysis guarantied the successful assembly of these Fe_3O_4/ZnO core-shell heterostructured nanoparticles.

Fe_3O_4/ZnMnS System

- Using the same synthetic route that was utilized to fabricate Fe_3O_4/ZnO core-shell heterostructured nanoparticles, Fe_3O_4/ZnMnS core-shell heterostructured nanoparticles were prepared (with minor modifications).
- Excellent matching by substituting paramagnetic Mn^{2+} ions by Zn^{2+} ions in the host ZnS and a very good adherence of doped-ZnS on the previously treated magnetite can be attributed, respectively, to the almost same order in the ionic radius and similar crystalline structures.
- The paramagnetic Mn^{2+} ion can generate a new energy level in the energy bands of this system which is evidenced from optical absorption and photoluminescence spectroscopy tests since the Fe_3O_4/ZnS nanoparticles do not exhibit any strong orange emission peak centered at ~ 598 nm.
- The existence of a slight ferromagnetic behavior at room temperature in this heterostructure may be due to the presence of a weak coercivity in the M-H curves and could be plausibly explained under the framework of the exchange mechanism between 3d electrons in the partially occupied 3d-orbitals of the Mn^{2+} ions and the magnetite nanocrystals.

5.2 Future Perspective

As it is known from the diverse biomedical applications using appealing quantum dots, these core-shell nanostructures could find potential usefulness in photodynamic therapy as carriers of photosensitizing agents. However, these nanoparticles must pass first through many tests such as further functionalization, thermodynamic stability, solubility in water, photo-oxidation, bioconjugation, etc. before being used *in vivo* tests. A first stage in a future work would be to carry out a suitable and facile functionalization of these Fe_3O_4/ZnO and Fe_3O_4/ZnMnS

nanoparticles in order to preserve their superparamagneto-luminescent properties for bioconjugation. Because these core-shell quantum dots were not synthesized in organic media, it is suggested to functionalize them as outside capping ligands appear due to the synthesis route. The functionalization would allow the covalent or non-covalent attachment of certain biomolecules onto the surface of quantum dots without reducing their quantum yield. Although the luminescence mechanism of ZnO is still controversial, a new bifunctional ligand (hydrophobic and/or hydrophilic) on their surface could produce more defects which make the drop of luminescence unavoidable.

On the other hand, for quantum dots synthesized in aqueous media we should attach non-common biomolecules such as antibodies or peptides to design fluorescent bioprobes. In addition, we can consider the hydrophilic ligands which appear onto the surface of these quantum dots to be used as stabilizers for the bioconjugation. Thus, these stabilizers and biomolecules might improve the bioconjugation but if many of them are added and react between themselves or with other organic molecules, the aggregation and consequently the precipitation would occur.

The conventional treatment of cancer (chemotherapy) could also be replaced by the photodynamic therapy which takes advantage of the interaction of photosensitizers and light to generate cytotoxic singlet oxygen and thus killing the cancer cells. However, these photosensitizing agents tend to aggregate in aqueous media and possess poor solubility. Then, we should invoke the excellent features of our core-shell systems to obtain good cell-penetrating properties and enhanced photochemical activity. In a joint effort with the Department of Chemistry, we were able to evaluate the singlet oxygen quantum yield of the Fe_3O_4/ZnO system obtaining a value of 0.28 in presence of 1,3-diphenylisobensofuran (DPBF), a singlet oxygen quencher, in methanol (see Table 3). But to make the core-shell quantum dots an ideal platform for photodynamic therapy, a complete study of the most relevant points to carry out the bioconjugation is needed. Note that these core-shell quantum dots could have access to deeper tumors since these can efficiently absorb at near regions where the tissue is much more transparent.

QDs/PS	PS	$^1O_2\ \Phi_\Delta$	Ref.
	Rose bengal	0.76	Rosa et al
	Methylene blue	0.5	Rosa et al
CdSe		0.05	Samia et.al
CdTe/dye		0.43	Shi et al
CdSe@CdS@ZnS/phitochelatin		0.31	Hsieh et al
Fe_3O_4/ZnO core-shell		0.28	Present work

Table 3: Comparison of the singlet oxygen quantum yield ($^1O_2\ \Phi_\Delta$) (PS: photosensitizer and QDs: quantum dots)

Reference

[1] Jiaqi Wan, Hui Li and Kezheng Chen, "Synthesis and characterization of Fe_3O_4/ZnO core-shell structured nanoparticles", *Mat. Chem. Phys.* (**2009**) 114: 30-32.

[2] Peng Zou, Xia Hong, Xueying Chu, Yajun Li and Yichun Liu, "Multifunctional Fe_3O_4/ZnO nanocomposites with magnetic and optical properties", *J. Nanosci. Nanotech.* (**2010**) 10: 1992-1997.

[**3**] Hong R. Y., Zhang S. Z., Di G. Q., Li H. Z., Zheng Y., Ding J., Wei D. G., "Preparation characterization and application of Fe_3O_4/ZnO core-shell magnetic nanoparticles" *Materials Research Bulletin* (**2008**) 43:2457-2468.